Monthly Notices
of the
ROYAL ASTRONOMICAL SOCIETY

MNRAS **439,** 1472–1493 (2014)
Advance Access publication 2014 February 7

doi:10.1093/mnras/stt2495

Spitzer Space Telescope spectra of post-AGB stars in the Large Magellanic Cloud – polycyclic aromatic hydrocarbons at low metallicities

Mikako Matsuura,[1⋆] Jeronimo Bernard-Salas,[2,3] T. Lloyd Evans,[4] Kevin M. Volk,[5] Bruce J. Hrivnak,[6] G. C. Sloan,[7] You-Hua Chu,[8] Robert Gruendl,[8] Kathleen E. Kraemer,[9] Els Peeters,[10,11] R. Szczerba,[12] P. R. Wood,[13] Albert A. Zijlstra,[14] S. Hony,[15] Yoshifusa Ita,[16] Devika Kamath,[13] Eric Lagadec,[7] Quentin A. Parker,[17,18,19] Warren A. Reid,[17] Takashi Shimonishi,[20] H. Van Winckel,[21] Paul M. Woods,[1,22] F. Kemper,[23] Margaret Meixner,[5] M. Otsuka,[23] R. Sahai,[24] B. A. Sargent,[25] J. L. Hora[26] and Iain McDonald[14]

[1]*Department of Physics and Astronomy, University College London, Gower Street, London WC1E 6BT, UK*
[2]*Department of Physical Sciences, The Open University, Milton Keynes, MK7 6AA, UK*
[3]*Institut d'Astrophysique Spatiale, CNRS/Université Paris-Sud 11, F-91405 Orsay, France*
[4]*SUPA, School of Physics and Astronomy, University of St Andrews, North Haugh, St Andrews, Fife KY16 9SS, UK*
[5]*Space Telescope Science Institute, 3700 San Martin Drive, Baltimore, MD 21218, USA*
[6]*Department of Physics and Astronomy, Valparaiso University, Valparaiso, IN 46383, USA*
[7]*Department of Astronomy, Cornell University, Ithaca, NY 14853, USA*
[8]*Department of Astronomy, University of Illinois at Urbana-Champaign, 1002 West Green Street, Urbana, IL 61801, USA*
[9]*Institute for Scientific Research, Boston College, Kenny Cottle L106B, Newton, MA 02459-1161, USA*
[10]*Department of Physics and Astronomy, University of Western Ontario, London, ON N6A 3K7, Canada*
[11]*SETI Institute, 515 North Whisman Road, Mountain View, CA 94043, USA*
[12]*N. Copernicus Astronomical Center, Rabianska 8, PL-87-100 Torun, Poland*
[13]*Research School of Astronomy and Astrophysics, Australian National University, Weston Creek, ACT 2611, Australia*
[14]*Jodrell Bank Centre for Astrophysics, School of Physics and Astronomy, University of Manchester, Oxford Road, Manchester M13 9PL, UK*
[15]*Max-Planck-Institute for Astronomy, Königstuhl 17, D-69117 Heidelberg, Germany*
[16]*Astronomical Institute, Graduate School of Science, Tohoku University, 6-3 Aramaki Aoba, Aoba-ku, Sendai, Miyagi 980-8578, Japan*
[17]*Department of Physics & Astronomy, Macquarie University, NSW 2109, Australia*
[18]*Research Centre in Astronomy, Astrophysics and Astrophotonics (MQAAAstro), Macquarie University, NSW 2109, Australia*
[19]*Australian Astronomical Observatory, PO Box 296, Epping, NSW 2121, Australia*
[20]*Department of Earth and Planetary Sciences, Graduate School of Science, Kobe University, Nada Kobe 657-8501, Japan*
[21]*Instituut voor Sterrenkunde, K.U.Leuven, Celestijnenlaan 200B, B-3001 Leuven, Belgium*
[22]*Astrophysics Research Centre, School of Mathematics and Physics, Queen's University Belfast, Belfast BT7 1NN, UK*
[23]*Academia Sinica, Institute of Astronomy and Astrophysics, 11F of ASMAB, AS/NTU, No. 1, Sec. 4, Roosevelt Rd, Taipei 10617, Taiwan, ROC*
[24]*Jet Propulsion Laboratory, MS 183-900, California Institute of Technology, Pasadena, CA 91109, USA*
[25]*Center for Imaging Science, Rochester Institute of Technology, 54 Lomb Memorial Drive, Rochester, NY 14623, USA*
[26]*Harvard–Smithsonian Center for Astrophysics, 60 Garden Street, MS 65, Cambridge, MA 02138-1516, USA*

Accepted 2013 December 28. Received 2013 December 18; in original form 2013 October 3

ABSTRACT

This paper reports variations of polycyclic aromatic hydrocarbons (PAHs) features that were found in *Spitzer Space Telescope* spectra of carbon-rich post-asymptotic giant branch (post-AGB) stars in the Large Magellanic Cloud (LMC). The paper consists of two parts. The first part describes our *Spitzer* spectral observing programme of 24 stars including post-AGB candidates. The latter half of this paper presents the analysis of PAH features in 20 carbon-rich post-AGB stars in the LMC, assembled from the Spitzer archive as well as from our own programme. We found that five post-AGB stars showed a broad feature with a peak at 7.7 μm, that had not been classified before. Further, the 10–13 μm PAH spectra were classified into

⋆E-mail: mikako@star.ucl.ac.uk

four classes, one of which has three broad peaks at 11.3, 12.3 and 13.3 μm rather than two distinct sharp peaks at 11.3 and 12.7 μm, as commonly found in H II regions. Our studies suggest that PAHs are gradually processed while the central stars evolve from post-AGB phase to planetary nebulae, changing their composition before PAHs are incorporated into the interstellar medium. Although some metallicity dependence of PAH spectra exists, the evolutionary state of an object is more significant than its metallicity in determining the spectral characteristics of PAHs for LMC and Galactic post-AGB stars.

Key words: stars: AGB and post-AGB – circumstellar matter – galaxies: individual: Large Magellanic Cloud – infrared: stars.

1 INTRODUCTION

The Large Magellanic Cloud (LMC) has attracted much attention in recent years, as its relative proximity (50 kpc; Westerlund 1997) and relatively low metallicity (about half of the solar metallicity; Olszewski, Suntzeff & Mateo 1996) make the LMC an important laboratory to examine the effects of metallicity on molecular and dust formation.

It is increasingly important to understand how different metallicities could impact on the physics and chemistry of the constituent stars and the interstellar medium (ISM) of galaxies. Different metallicities might result in different compositions of dust and molecules, changing the spectra of stars and the ISM as well as those of the integrated light of galaxies. A set of features which are often found in the spectra of stars, the ISM and galaxies have been attributed to polycyclic aromatic hydrocarbons (PAHs). Madden et al. (2006) found that PAH features were less pronounced in low-metallicity dwarf galaxies. Similarly, the Spitzer Infrared Nearby Galaxies Survey (SINGS) of 67 galaxies within 3–25 Mpc (Kennicutt et al. 2003) showed that PAH features were weaker in galaxies of lower metallicity (Draine et al. 2007). In contrast, PAH features of planetary nebulae (PNe) showed no difference between the Milky Way (MW), the LMC and the Small Magellanic Cloud (SMC; Bernard-Salas et al. 2009), despite the LMC and the SMC having about half and a quarter of the solar metallicity, respectively. It is still unclear how low metallicities affect PAHs in stars and the ISM in a different manner.

It has been proposed that carbon-rich asymptotic giant branch (AGB) stars are an ideal site for PAH formation (Allamandola, Tielens & Barker 1989). Carbon atoms are synthesized in stellar interiors during the AGB phase, and are dredged-up to the outer layers of the star (Herwig 2005). Although the atmospheres of AGB stars contain more oxygen than carbon initially, successive dredge-ups will increase the abundance of carbon, resulting in more carbon than oxygen in some stars within a certain mass range (Vassiliadis & Wood 1993). Carbon and oxygen atoms in stellar atmospheres bond to form CO first, and excess carbon atoms are available to form other carbon-bearing molecules. One of the key molecules in carbon-rich chemistry is C_2H_2, which is thought to be the parent molecule in the formation of PAHs (Allamandola et al. 1989; Cherchneff, Barker & Tielens 1992). A sequence of C_2H_2 added on to carbon and a hydrogen chain forms aromatic hydrocarbons; further additions of C_2H_2 and C_4H_2 form larger PAHs. As the abundance of C_2H_2 in AGB atmospheres is metallicity dependent (Matsuura et al. 2005), the formation of PAHs in carbon-rich AGB stars could also depend on metallicity.

In general, PAHs are rarely seen in the spectra of AGB stars (Sloan et al. 2007). Only when the effective temperature of the central star increases in the post-AGB phase and subsequent PN phase do PAHs appear in their spectra. This is because PAHs require energy supplied by UV or optical radiation to emit their infrared (IR) spectra (Leger & Puget 1984; Allamandola et al. 1989; Sloan et al. 2007). Thus, in order to investigate PAHs immediately after their formation, we have chosen to study PAHs in post-AGB stars.

PAHs exhibit a variety of spectral features. The *Infrared Space Observatory* (*ISO*) observations of Galactic objects showed that PAH spectral profiles in the 6–9 and 10–15 μm regions vary among objects (e.g. H II regions, PNe, post-AGB stars; Hony et al. 2001; Peeters et al. 2002). In the 10–15 μm region, there are two strong peaks located at 11.3 and 12.7 μm, and the relative intensity of the 11.3 μm feature over that at 12.7 μm spans a factor of 7. Hony et al. (2001) suggested that the change of the 10–15 μm profile should be caused by the different structures and compositions of PAHs. In the meantime, Peeters et al. (2002) found that most profiles of the 6–9 μm features fall into three groups, which are correlated with object type. Peeters et al. (2002) suggested that nitrogenation causes the shift of the peaks of the 6–9 μm feature. Alternatively, it has been proposed that aliphatic carbon could further contribute to the spectral variations in the 6–9 μm feature (e.g. Sloan et al. 2007; Kwok & Zhang 2011; Carpentier et al. 2012). Further, hydrogenation should also contribute to the variation (Duley & Williams 1981; Jones, Duley & Williams 1990). The cause of spectral variations at 6–9 μm is still unsettled.

This paper focuses on mid-infrared (mid-IR) spectra of PAHs found in post-AGB stars in the LMC. Our objectives are to search for any difference in PAH profiles between the LMC and the MW, and to examine whether the differences in PAH profiles may be caused by the metallicity difference. The first part (Sections 2– 4) of this paper outlines our *Spitzer* observing programme of post-AGB stars in the LMC. We selected post-AGB candidates in the LMC using several different criteria, including position in colour–colour and colour–magnitude diagrams, and we will verify these selection methods. The second part (Section 5) is the investigation of PAH features in post-AGB stars. For this analysis, archival data are added in addition to our own *Spitzer* observations. LMC post-AGB stars show more spectral variations of PAHs than are known from Galactic counterparts. We discuss the possible causes of these variations.

2 *SPITZER* CYCLE-5 OBSERVING PROGRAMME

2.1 Target selection

Our primary targets were post-AGB candidates in the LMC. Additionally, we included a few candidate AGB stars and PNe, in order to examine the spectral evolution from the AGB phase through the post-AGB phase to the PN phase.

Table 1. List of targets.

No.	Object name	AOR	SAGE coordinates (J2000)		Selection[a]	Date[b]	Mode/exp. time	Obj. class.[c] Our work	Spt./obj. class[d] Literature
1	IRAS 04518−6852	27985664	$04^h51^m40^s.56$	$-68^d47^m34^s.9$	SAGE	04-29	SH (120 s×6)	C AGB	C AGB[1]
2	IRAS F04540−6721	25996800	$04^h54^m03^s.62$	$-67^d16^m18^s.2$	(iii)	04-28	SL (14 s×3), LL(6 s×3)	YSO/H II	Em[2]
3	IRAS 04589−6547	25997056	$04^h59^m07^s.39$	$-65^d43^m13^s.3$	(iii)	04-28	SL (60 s×3), LL(6 s×3)	O/B supergiant	O9ep/B1-2ep[3, 2]
4	IRAS 05026−6809	25991680	$05^h02^m31^s.47$	$-68^d05^m35^s.8$	(i)	04-28	SL2 (60 s×3), SL1 (14 s×3), LL (6 s×3)	C AGB	C AGB[4], ERO[5]
5	IRAS 05053−6901	25991168	$05^h05^m04^s.81$	$-68^d57^m48^s.3$	(iv)	04-28	SL (14 s×3), LL(14 s×3)	C AGB	
6	MSX LMC 130	25991936	$05^h07^m18^s.33$	$-69^d07^m42^s.9$	(v)	04-28	SL (14 s×3), LL(30 s×3)	O post-AGB	A7II/A9I[3], A7e[2]
7	MSX LMC 92	25990656	$05^h08^m25^s.59$	$-68^d53^m59^s.9$	(v)	04-28	SL (14 s×3), LL(30 s×3)	C AGB	C[2]
8	IRAS 05092−7121	25992448	$05^h08^m35^s.92$	$-71^d17^m30^s.7$	(i)	04-29	SL (14 s×3), LL(14 s×3)	C post-AGB	late B–early G + Hα em.[2]
9	IRAS 05110−6616	25992704	$05^h11^m10^s.65$	$-66^d12^m53^s.7$	(i)	04-27	SL (14 s×3), LL(14 s×3)	C post-AGB	F3II(e)[3]
10	IRAS 05189−7008	25996288	$05^h18^m25^s.67$	$-70^d05^m32^s.6$	(iii)	04-29	SL (60 s×3), LL(6 s×3)	C AGB	
11	J052043.58−692341.4	27985920	$05^h20^m43^s.58$	$-69^d23^m41^s.4$	(ii)	04-29	SL (60 s×3), LL(14 s×3)	C post-AGB	F5Ib(e)[3]
12	MSX LMC 439	25990400	$05^h20^m48^s.21$	$-70^d12^m12^s.5$	(v)	04-28	SL (14 s×3), LL(30 s×3)	R CrB	R CrB[6]
13	SMP LMC 52	25996544	$05^h21^m23^s.83$	$-68^d35^m33^s.5$	(iii)	04-29	SL (60 s×15), LL(30 s×3)	C PN	C PN[7, 8, 9]
14	J052520.75−705007.3	25996032	$05^h25^m20^s.75$	$-70^d50^m07^s.3$	(iii)	04-28	SL (60 s×3), LL(14 s×3)	C post-AGB	A1Ia[3], F2-F5I[2]
15	MSX LMC 474	25992192	$05^h25^m51^s.85$	$-68^d46^m34^s.3$	(v)	04-29	SL (14 s×3), LL(14 s×3)	C AGB	
16	MSX LMC 736	25993216	$05^h33^m06^s.80$	$-70^d30^m34^s.9$	(v)	04-28	SH (120 s×6)	C AGB	
17	J053336.37−692312.7	27985408	$05^h33^m36^s.07$	$-69^d23^m12^s.7$	(ii)	04-28	SL (14 s×3), LL(14 s×3)	O post-AGB	G8pe[3]
18	SMP LMC 75	25993984	$05^h33^m46^s.99$	$-68^d36^m44^s.2$	(iv)	04-29	SL1 (14 s×3), LL (14 s×3), SH(120 s×10)	C PN	PN[7, 8, 9]
19	J053911.60−693125.6	25995776	$05^h39^m11^s.60$	$-69^d31^m25^s.6$	(iii)	04-29	SL1 (60 s×18), LL(30 s×4)	Unclassified	
20	J053941−692916	27986176	$05^h39^m41^s.08$	$-69^d29^m16^s.7$	YSO	04-28	SL (14 s×3), LL1(14 s×3), SH(120 s×10)	YSO	YSO[10]
21	J054055.81−691614.6	25995520	$05^h40^m55^s.81$	$-69^d16^m14^s.6$	(iii)	04-29	SL (60 s×15), LL(14 s×3)	O/B supergiant	O–B[3], O–Bpe[2]
22	MSX LMC 1795	25990912	$05^h42^m21^s.90$	$-69^d02^m59^s.1$	(iv)	04-28	SL (14 s×3), LL(30 s×4)	R CrB	R CrB cand.[6], C[2]
23	IRAS 05509−6956	25991424	$05^h50^m26^s.30$	$-69^d56^m02^s.8$	(i)	03-06	SL (6 s×3), LL(6 s×3)	C AGB	
24	IRAS 05588−6944	25992960	$05^h58^m25^s.97$	$-69^d44^m25^s.3$	(i)	04-28	SL (6 s×3), LL1(6 s×3), LL2(14 s×3)	C post-AGB	WC?[3]

[a]The selection methods as described in Section 2.1. SAGE: observed by the SAGE-spec project (Kemper et al. 2010). YSO: follow-up of *Akari* YSO studies (Shimonishi et al. 2008).
[b]Observed dates in 2009 and mm-dd format.
[c]The object classifications based on our work.
[d]Spectral types or object types (R CrB/PNe) from the literature, [1] Woods et al. (2011), [2] this work, [3] van Aarle et al. (2011), [4] van Loon et al. (2006), [5] Gruendl et al. (2008), [6] Soszyński et al. (2009), [7] Jacoby (1980), [8] Sanduleak, MacConnell & Philip (1978), [9] Leisy & Dennefeld (1996) and [10] Shimonishi et al. (2008).

Although theoretically the post-AGB phase is well defined as the transition phase between the AGB and the PN phases, there are several observational characteristics that could match the theoretical definition. We employed three different selection approaches for post-AGB candidates: (a) a selection based on IR colour–colour–magnitude diagrams; (b) a selection of stars with double-peaked spectral energy distributions (SEDs); (c) a selection of stars which were identified as post-AGB candidates in the literature. The identifications of post-AGB stars in the literature were based on combinations of IR colours, optical spectra, luminosities and light curves. Within our team, we searched for candidates independently with five different selection criteria, and created a combined sample. The selection criteria are briefly described below, and the method applied to a specific target is indicated in Table 1. Later in this paper, we will re-examine these selection criteria based on colours. We restricted our sample to [8.0]<8, where [8.0] is the magnitude at 8.0 μm, in order to obtain a good signal-to-noise (S/N) ratio.

(i) Extremely red objects (EROs). As their name implies, EROs are very red at mid-IR wavelengths. Gruendl et al. (2008) defined EROs to have *Spitzer* colours of [4.5]–[8.0] > 4.0, where [4.5] and [8.0] are magnitudes in the 4.5 and 8.0 μm bands in the *Spitzer* LMC Point Source Catalog [Surveying the Agents of Galaxy Evolution (SAGE); Meixner et al. 2006]. These EROs are stars which are heavily obscured by dust, and they are probably related with mass-loss at the late AGB phase. Some of the EROs show double-peaked SEDs (Gruendl et al. 2008), suggesting that the extensive mass-loss rate of the AGB phase has terminated, and the star has entered the post-AGB phase. Five EROs were observed.

(ii) van Aarle et al. (2011) selected 70 probable post-AGB candidates. They initially selected stars as potential candidates on the basis of their [8]–[24] colour, and narrowed down the list of candidates by the SEDs, luminosities and optical spectra. From these candidates, we chose one source with a 'circumbinary disc' (J053336.37−692312.7), and one source with a 'steady state expanding shell' (J052043.58−692341.4).

(iii) Galactic post-AGB stars can indicate the typical IR colours expected for LMC post-AGB stars. Szczerba et al. (2007) assembled a list of Galactic post-AGB stars, some of which have *ISO*/the Short Wavelength Spectrometer (SWS) spectra (Sloan et al. 2003). These spectra were convolved with the *Spitzer* and 2MASS filter transmission curves, producing synthetic IR colours of post-AGB objects. We plotted K–[24] and K–[8.0] colours of Galactic post-AGB stars and selected two SAGE LMC post-AGB candidates which have similar colours to Galactic post-AGB stars.

(iv) Two stars (MSX SMC 29 and SMP LMC 11) in the Magellanic Clouds were identified as carbon-rich post-AGB stars based on their *Spitzer* spectra (Bernard-Salas et al. 2006; Kraemer et al. 2006). Their magnitudes and colours indicated [8]<8, J–[8.0] > 5 and [8]–[24] > 0.5, and we selected seven stars which met these criteria from the SAGE catalogue (Meixner et al. 2006).

(v) Wood & Cohen (2001) identified LMC post-AGB candidates from the *MSX* IR survey (Egan, Van Dyk & Price 2001) and massive compact halo objects (MACHOs) project's light curves (Alcock et al. 2001). We included five targets from Wood & Cohen (2001). These targets were selected for a variety of reasons. MSX LMC 130 had an intermediate oxygen-rich optical spectral with emission lines. MSX LMC 736 showed an early M spectral type, slowly declining magnitudes and a very bright mid-IR SED though later the M-type star turned out to be a foreground M dwarf coincident with a dusty carbon-rich star. MSX LMC 439 is an R CrB star with a characteristic R CrB light curve, and the other two stars had near-infrared (near-IR) to mid-IR SEDs indicating likely binary post-AGB stars (Van Winckel 2003).

In addition to the above selections for low-resolution spectral targets, we selected three targets for high-resolution spectra, in order to identify narrow molecular and ice features. Kemper et al. (2010) have taken low-resolution Infrared Spectrograph (IRS) spectra of about 200 point sources in the LMC. Low-resolution spectra of one object (IRAS 04518−6852) gave a hint of molecular features from 10–15 μm, so we requested follow-up observations with higher spectral resolution. The second is a young stellar object (YSO), J 053941−692916 identified by an ice band in an *Akari* spectrum (Shimonishi et al. 2010). The last one (SMP LMC 75) had a similar mid-IR colour to a molecular-rich post-AGB star in the LMC (Kraemer et al. 2006).

2.2 Observations and data reduction

We observed 24 post-AGB candidates, late-phase AGB stars and PNe with the IRS (Houck et al. 2004) on board the *Spitzer Space Telescope* (Werner et al. 2004). The programme ID was 50338. The observations were made between 2009 March 6 and April 29. We mainly used the low-resolution IRS modules, consisting of short low (SL) and long low (LL), except for three sources, which were observed with the high-resolution modules using short high (SH) and long high. Table 1 gives the dates and integration times for each module, SAGE coordinates and Astronomical Observation Request (AOR) numbers.

The data were processed using the *Spitzer* Science Center (SSC)'s pipeline (version 18.7), which was maintained at Cornell, with the SMART reduction package (Higdon et al. 2004; Lebouteiller et al. 2010). The basic calibrated data were used. The reduction steps began with removing and replacing unstable sensitive pixels (rogue pixels) using the SSC tool irsclean. The next step was averaging the individual exposures for each module. Fringes were present in the LL1 module (20–24 μm) in four objects, and were removed using the defringe tool in SMART. For the high-resolution modules, the spectra were extracted using full aperture extraction. For the low-resolution modules, the background was removed by subtracting the averaged intensities at two off-target nod positions for a given module. The low-resolution spectra were extracted using tapered column extraction with a slit width of 4 pixels. For 10 faint objects, an advanced optimal extraction algorithm (Lebouteiller et al. 2010) was applied, though the results of these two extractions were nearly identical in the end. It is worth mentioning that five objects in the low-resolution observations exhibited either additional sources and/or complex structure within the slit. For four sources, manual optimal extraction was performed to properly isolate the sources and the background, while one source did not require this process. For these five sources the background was removed by subtracting the slit-order position as opposed to the nod position.

Fig. 1 shows the SEDs of our targets. The SEDs were constructed using photometric data from 2MASS (Skrutskie et al. 2006), the InfraRed Survey Facility (IRSF; Kato et al. 2007), SAGE (Meixner et al. 2006) and our *Spitzer* IRS spectra. Our primary targets were dust-embedded objects, whose SEDs peak at 10–20 μm. About half (13 objects) of the targets have double-peaked SEDs; the first peak is at near-IR wavelengths or shorter and the second peak at mid-IR wavelengths. The first peak likely corresponds to the stellar component, and the second peak corresponds to the thermal dust emission from the circumstellar envelope. The low-resolution spectra of IRAS 04518−6852 and MSX LMC 736 were taken from the SAGE-Spec project (Kemper et al. 2010).

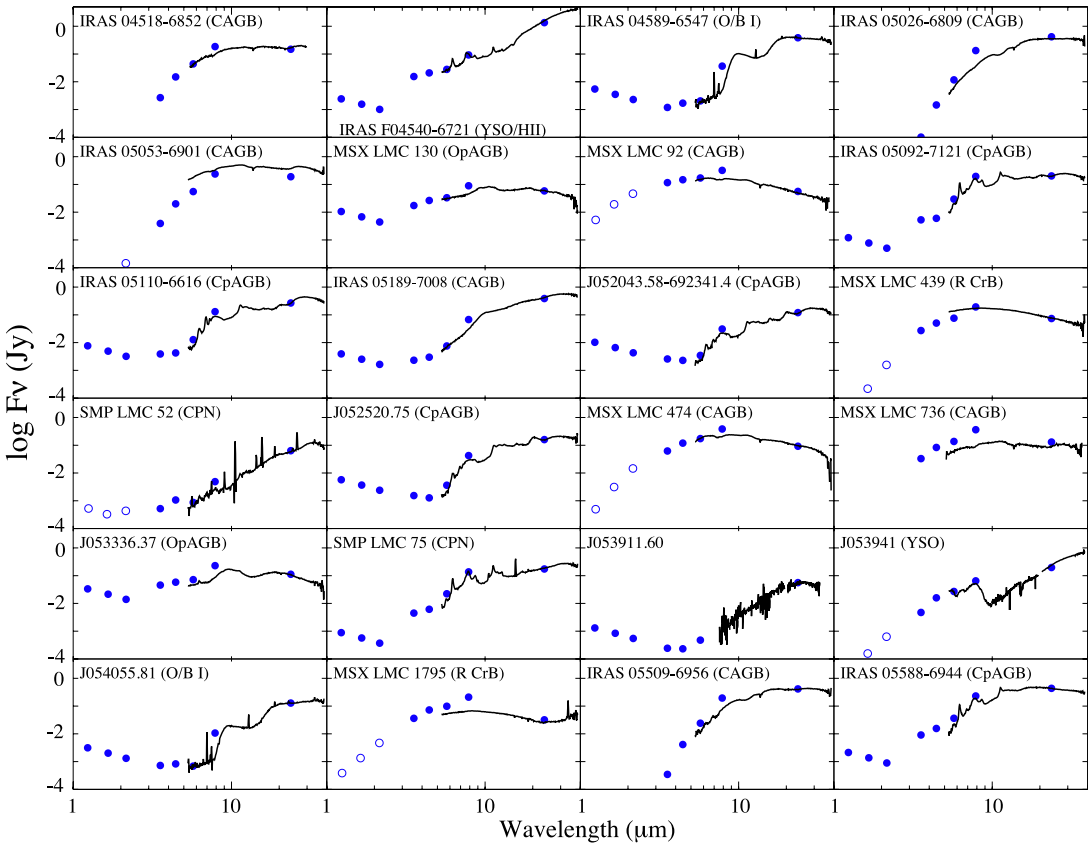

Figure 1. IR SEDs of our targets. *Spitzer* IRS spectra are plotted as black lines, accompanied by *Spitzer*-SAGE and 2MASS photometric points as blue filled circles. Photometric data from the IRSF are plotted as open circles.

The 2MASS photometry for IRAS 05189−7008 and MSX LMC 736 could not be used in Fig. 1 because of contributions from nearby field stars that are coincidentally located close to the carbon-rich AGB stars (Appendix C).

Gruendl & Chu (2009) have listed IRAS 05189−7008 as a YSO, because this object shows unusual colours and magnitudes as AGB stars do, and because its colour and magnitude could be closer represented by YSOs. Our *Spitzer* IRS spectrum shows that this star is one of the reddest carbon stars with very weak molecular and dust features, and IRAS 05189−7008 pushes the limits of the carbon-rich AGB star boundaries pertaining to the colour–magnitudes and colour–colour beyond the known range.

3 SPECTRA AND OBJECT CLASSIFICATIONS

The *Spitzer* spectra of 24 targets were classified according to the object types. We found AGB stars, post-AGB stars, PNe, YSOs/H II regions and O/B supergiants. Hereafter, we treated R CrB stars separately from post-AGB stars, because their spectra are different. We describe the spectra and the reason for object classifications in the following subsections, and list object classifications in Table 1.

3.1 Carbon-rich AGB stars

IR spectra of carbon-rich AGB stars are characterized by C_2H_2 and HCN absorption bands at 7 and 14 μm (e.g. Aoki, Tsuji & Ohnaka 1999) together with SiC feature at 11.3 μm (e.g. Zijlstra et al. 2006). The SiC dust feature is normally found in emission, but has also been found in absorption in a few objects (Gruendl et al. 2008; Speck et al. 2009). Some carbon-rich AGB stars show a very broad emission feature at 30 μm (Zijlstra et al. 2006), which is often attributed to MgS dust (Hony et al. 2001), but the origin is still being debated (Volk et al. 2002; Messenger, Speck & Volk 2013). No PAHs or ionized lines are found, and the SEDs usually display a single peak.

Carbon-rich AGB stars are the most common objects among our targets, with eight stars, as summarized in Table 1. This is a consequence of many factors. Stellar evolution models predict that the lifetime of post-AGB phase is shorter than that of AGB stars, so that more AGB stars are expected than post-AGB stars (Vassiliadis & Wood 1993, 1994). The LMC has more carbon-rich AGB stars than oxygen-rich AGB stars (Westerlund 1997).

Carbon-rich AGB spectra from our sample are shown in Fig. 2. One can see the variation in the strengths of the C_2H_2 absorption features, which has a sharp Q-band branch feature at 13.7 μm, accompanied with a broad wing formed by the P and R branches (Matsuura et al. 2006). The SiC feature, which appeared in emission in most of the objects, is particularly strong in IRAS 05053−6901, whereas the SiC feature was found in absorption in IRAS 05026−6809 and IRAS 05509−6956. The spectrum of IRAS 05189−7008 has a weak SiC absorption. There are six objects that show the broad 30 μm feature (IRAS 05189−7008, IRAS 05026−6809, IRAS 05509−6956, IRAS 05053−6901, IRAS 04518−6852 and MSX LMC 736).

In Fig. 2, the low-resolution spectrum of IRAS 04518−6852 was taken from the SAGE-Spec project (Kemper et al. 2010), and the high-resolution spectrum was from our programme.

3.2 Carbon-rich PNe

Carbon-rich PNe show emission lines, and lines detected include 6.99 μm [Ar II], 12.81 μm [Ne II] and 33.48 μm [S III] lines. A dust continuum is often found, but not always (Stanghellini et al. 2007;

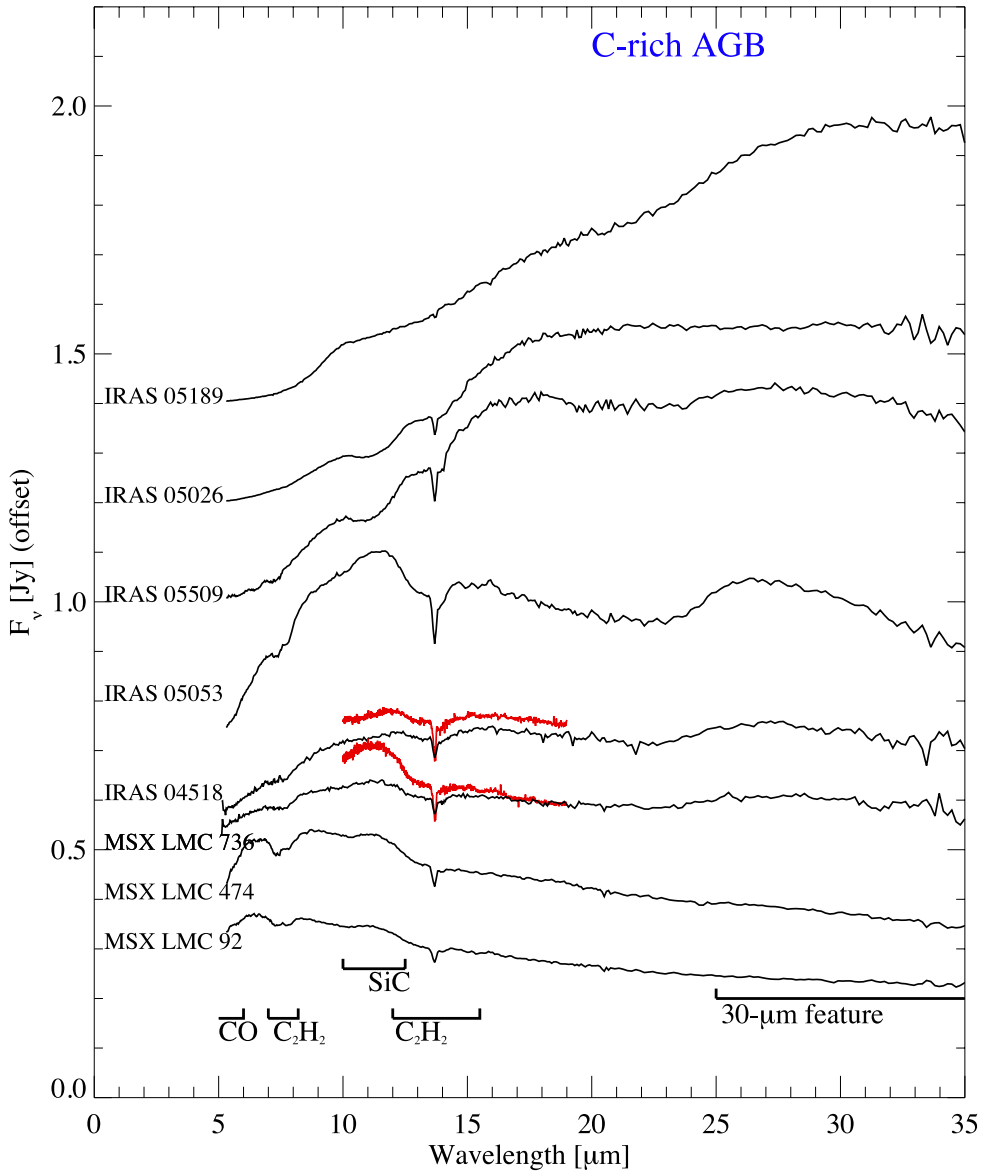

Figure 2. Spectra of C-rich AGB stars observed in the LMC. The molecular (C_2H_2 and CO) and dust (SiC and 30 μm) features are indicated. Fluxes are offset by arbitrary amounts for clarity. High-resolution spectra of IRAS 04518−6852 and MSX LMC 736 are plotted in red lines. The spectra are plotted in order of the underlying continuum temperature, from cooler (top) to warmer (bottom).

Bernard-Salas et al. 2009), and PAH features are also often found. SiC emission is occasionally found in LMC PNe, although it has rarely been found in Galactic PNe (Bernard-Salas et al. 2009; Speck et al. 2009).

Our sample contains two C-rich PNe, SMP LMC 52 and SMP LMC 75; their spectra are shown in Fig. 3. The 30 μm feature, which is associated with carbon-rich objects, is found in both spectra. SMP LMC 75 shows PAH features, including the one at 17.5 μm (Boersma et al. 2010). SMP LMC 52 has only the 30 μm feature as an indicator of carbon-rich nature, and it does not show PAHs. SMP LMC 52 is a high-excitation PN, indicated by the detection of [O IV] and [Ne V] lines (Bernard-Salas et al. 2009).

3.3 Carbon-rich post-AGB stars

As transitional objects from the AGB phase to the PN phase, carbon-rich post-AGB stars often show PAHs.

We classified five targets (IRAS 05092−7121, IRAS 05110−6616, J052043.58−692341.4, J052520.75−705007.3 and IRAS 05588−6944) as carbon-rich post-AGB stars, and their spectra are presented in Fig. 4. These spectra show PAHs, and four out of the five spectra exhibit both the 21 and 30 μm features. IRAS 05588−6944 is an exception, showing a rapid rise of the continuum up to 16 μm and then a gradual decline, with perhaps the 30 μm feature but no 21 μm feature. An unidentified feature at 15.8 μm, which may be associated with PAHs (Moutou, Léger & D'Hendecourt 1995; Van Kerckhoven et al. 2000), also appears in some post-AGB stars.

The unidentified '21 μm feature' has been found only in carbon-rich post-AGB stars. So far its detection has been reported in 16 Galactic stars (Hrivnak, Volk & Kwok 2009; Cerrigone et al. 2011), and a similar number (in total 11) of '21 μm feature' objects have been found in the Magellanic Clouds (Volk et al. 2011). Hrivnak et al. (2009) suggested that the 21 μm feature is related

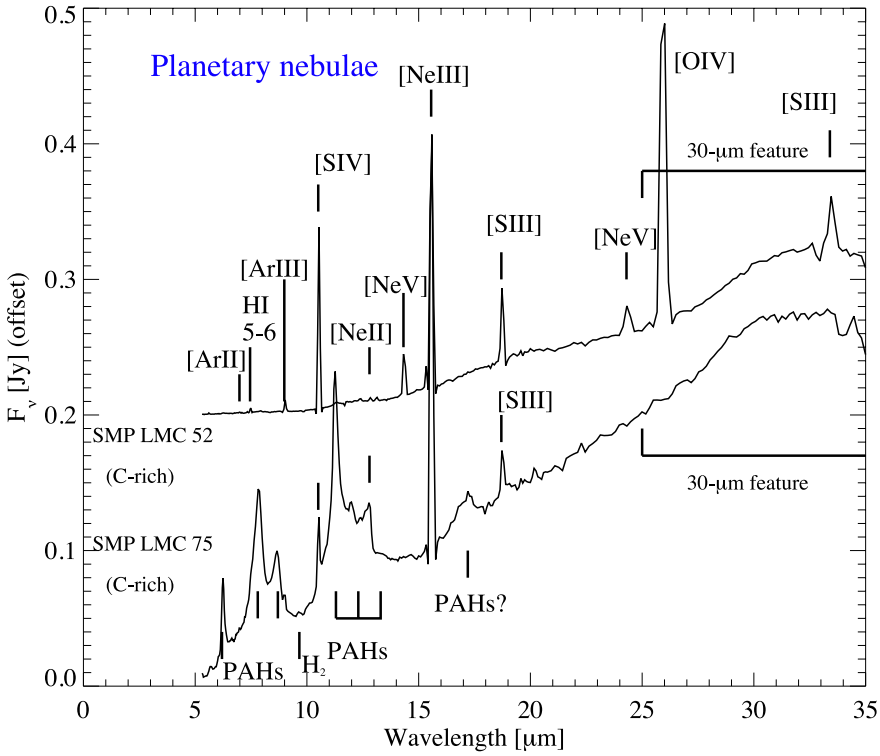

Figure 3. Spectra of the carbon-rich PNe observed in the LMC. The spectrum of SMP LMC 75 shows PAHs, indicating that this PN is carbon rich. SMP LMC 52 shows little sign of PAHs in the *Spitzer* spectrum, but the presence of the 30 μm feature shows the carbon-rich nature of this star.

with carbonaceous molecules or dust, while Li, Liu & Jiang (2013) proposed that it could be due to FeO. The identification of this feature is not yet well settled.

IRAS 05588−6944 is a peculiar object in our sample in several respects. van Aarle et al. (2011) studied the optical spectrum and the SED of IRAS 05588−6944 as part of the LMC post-AGB study, and assigned IRAS 05588−6944 to be a carbon sequence Wolf–Rayet (WC) candidate. They estimated the luminosity of IRAS 05588−6944 to be 13 000 $L_{\odot}$, which is within the post-AGB luminosity limit (35 000 $L_{\odot}$; van Aarle et al. 2011), but the optical spectral classification of WC did not fit the post-AGB criteria. Their fig. C.2 showed the optical spectrum of IRAS 05588−6944, showing He I and C II lines but no hydrogen recombination lines. The presence of carbon lines but a lack of hydrogen lines might suggest a WC nature. However, the optical spectrum is not typical of WC stars with a circumstellar envelope, which are usually classified as WC9 or WC10. van Aarle et al. (2011) pointed out that its optical spectrum lacked 5696 Å C III, which is commonly found in WC10 stars (Crowther, De Marco & Barlow 1998). The IR spectra of Galactic WC9 stars do not show PAHs (van der Hucht et al. 1996; Smith & Houck 2001) but that of IRAS 05588−6944 shows strong PAH features (Fig. 4). No recombination lines nor ionized lines have been detected in the IR spectrum of IRAS 05588−6944, even though such lines, indicative of an ionized nebula, have been found in IR WC spectra (van der Hucht et al. 1996; Smith & Houck 2001). The *Spitzer* spectrum IRAS 05588−6944 is compared with that of the Galactic post-AGB star IRAS 09470−4617, which is scaled by a factor of 0.11 in Fig. 5. The *Spitzer* spectrum of IRAS 09470−4617 is from Cerrigone et al. (2009), and they also have optical spectra. These two spectra look similar including the overall continuum, PAH features between 5 and 9 μm and the lack of 21 μm. Both show C II in the optical spectra. It seems that IRAS 05588−6944 and IRAS 09470−4617 could belong to a distinct class with a carbon-rich shell.

3.4 Oxygen-rich post-AGB stars

We found two oxygen-rich objects among our targets, and they are most likely post-AGB stars, because the spectral types of the central stars are A and G (Table 1), and because their SEDs are double peaked (Fig. 1).

Fig. 6 shows spectra of two oxygen-rich stars. Both of them show amorphous silicates, and MSX LMC 130 shows hints of crystalline silicates.

The PAH features detected in the spectrum of J053336.37−692312.7 are likely to be associated with the star itself. Along the IRS slit, PAH emissions are found only from the location of this star. J053336.37−692312.7 is probably a mixed-chemistry object, which has both oxygen-rich and carbon-rich molecules and dust in a single star. Waters et al. (1998) proposed that a circumbinary disc may be responsible for some cases of mixed chemistry: oxygen-rich dust had been ejected by the AGB star in the past and stored in the binary disc, while more recent mass-loss was carbon rich. van Aarle et al. (2011) suggested that the SED of J053336.37−692312.7 can be modelled well as a post-AGB star with a circumbinary disc. It seems possible that mixed chemistry in this object is related to the presence of the disc. Galactic post-AGB stars with mixed chemistry tend to have silicates with weak PAHs, and often crystalline silicates were more prominent than amorphous silicates (Molster, Waters & Tielens 2002; Matsuura et al. 2004; Perea-Calderón et al. 2009; Gielen et al. 2011). In contrast, LMC post-AGB stars with mixed chemistry tend to show stronger amorphous silicate features than crystalline silicate ones, or even no indication of crystalline silicates (Buchanan et al. 2009). Jones et al. (2013) proposed that

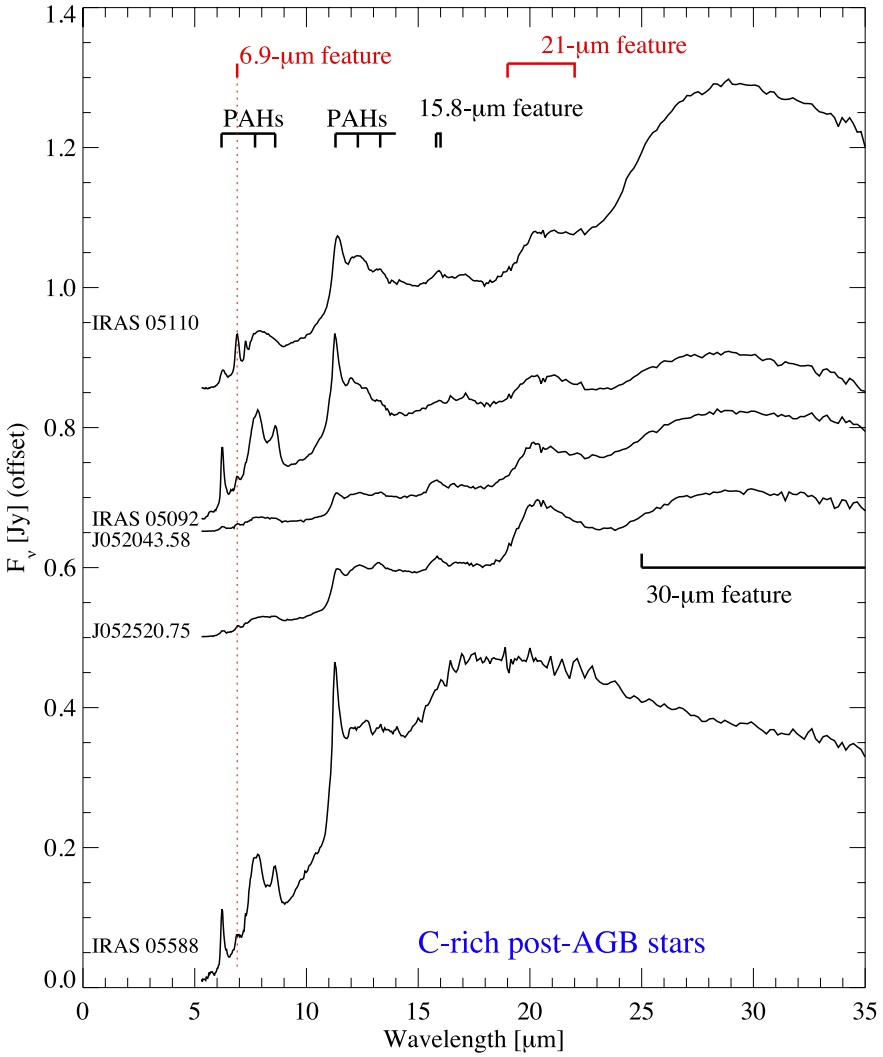

Figure 4. Spectra of carbon-rich post-AGB stars in the LMC. The approximate wavelengths of PAH features and four unidentified features (6.9, 15.8, 21 and 30 μm features) are indicated.

metallicity differences might affect the crystalline silicate compositions, and one could assume that the detection rate of crystalline silicates could also be affected by metallicity.

3.5 O/B supergiants

J054055.81−691614.6 and IRAS 04589−6547 are late O or early B-type stars (van Aarle et al. 2011). We discuss their optical spectra in more detail in Appendix C. The *Spitzer* spectra of these two stars show a series of ionized lines, including forbidden lines, and strong silicate emission bands at 10 and 18 μm (Fig. 7), indicating the presence of dust in their circumstellar envelopes. The mid-IR spectra of J054055.81−691614.6 and IRAS 04589−6547 resemble those of B[e] stars (Voors, Waters & Morris 1999; Kastner et al. 2006) and luminous blue variables (LBVs; Morris et al. 1999; Voors et al. 2000); both types of star have spectra with strong silicate emission bands and ionized lines. However, these two O/B supergiants do not appear to be either B[e] stars or LBVs. B[e]-type stars have forbidden emission lines of [Fe II] and [O I] in their optical spectra and circumstellar dust emission in their mid-IR spectra (Allen & Swings 1976; Lamers et al. 1998). However, the optical spectra of J054055.81−691614.6 and IRAS 04589−6547 do not show either [Fe II] or [O I] lines, so

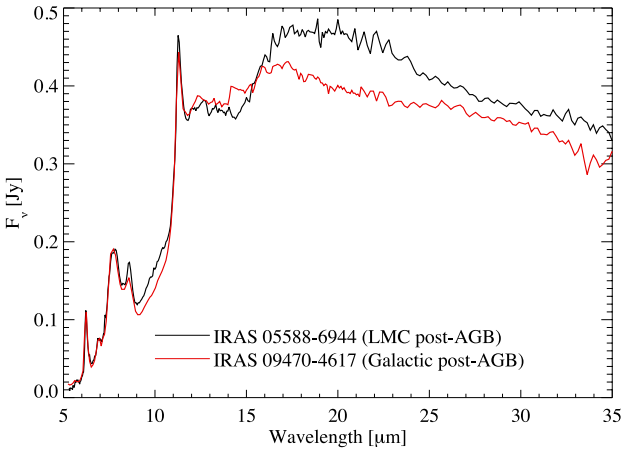

Figure 5. Comparison of IR spectra of a peculiar LMC post-AGB IRAS 05588−6944, with IRAS 09470−4617.

that they cannot be classified as B[e]-type stars. Furthermore, the luminosities of IRAS 04589−6547 and J054055.81−691614.6 were estimated to be 60 000 and 70 000 $L_{\odot}$, respectively, (van Aarle et al. 2011), corresponding to about $M_{\rm bol} \sim -7$. These luminosities

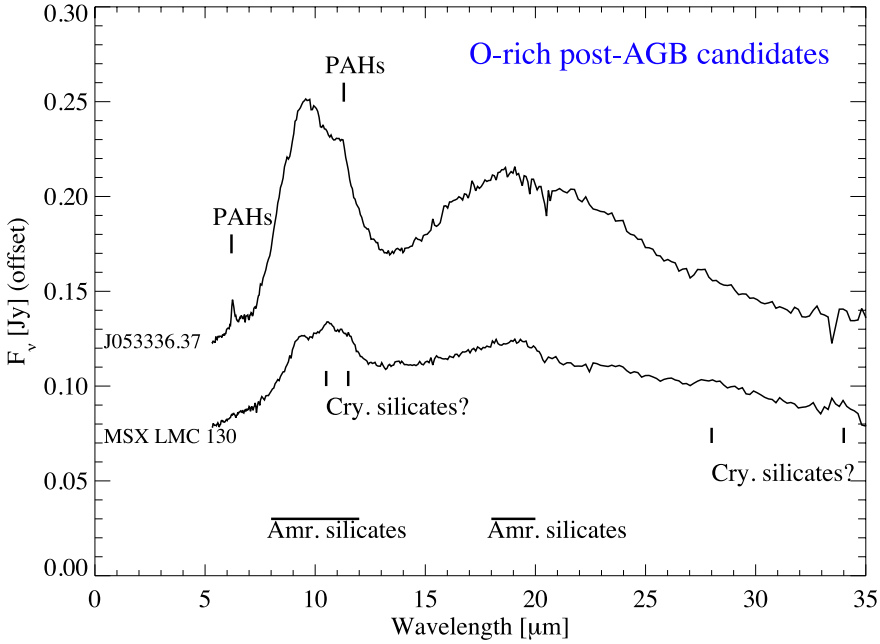

Figure 6. Oxygen-rich post-AGB candidates. Fluxes were offset by arbitrary amounts for clarity. Amorphous (Amr.) and potentially crystalline (Cry.) silicates were detected. PAHs in the spectrum of J053336.37−692312.7 are associated with the star itself rather than originating in the ISM.

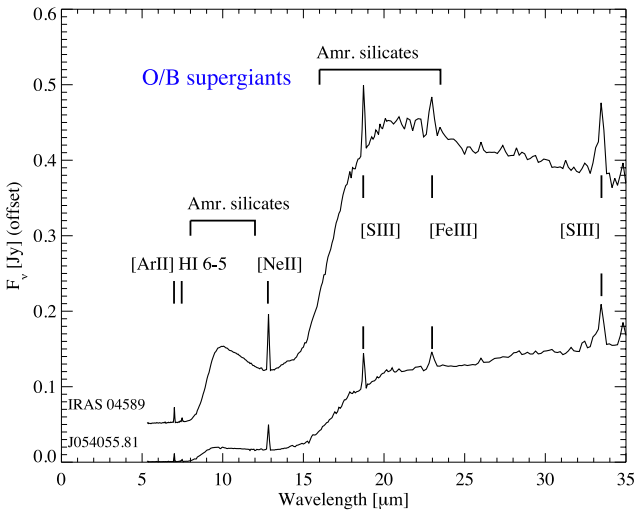

Figure 7. Spectra of the O/B supergiants with circumstellar envelopes. Strong amorphous silicate emission and ionized lines were detected.

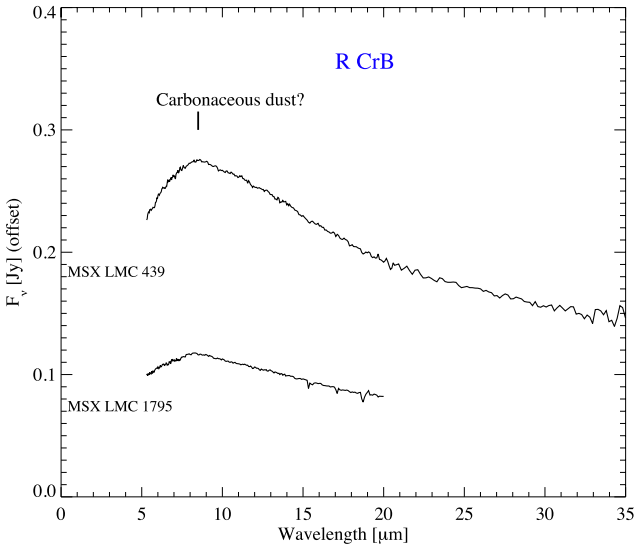

Figure 8. Spectra of the R CrB stars, MSX LMC 439 and MSX LMC 1795. Thermal emission from circumstellar dust is apparent.

are not sufficiently high to be LBVs, which have typical luminosities of −8.5 to −11 M_{bol} (Humphreys & Davidson 1994). Thus, IRAS 04589−6547 and J054055.81−691614.6 appear to be O/B supergiants that have hot circumstellar envelopes, but do not match known O/B supergiant or hypergiant categories with circumstellar envelopes, such as B[e]-type stars and LBVs.

3.6 R CrB stars

Two stars in our sample are an R CrB star and an R CrB candidate. MSX LMC 439 and MSX LMC 1795 were classified as R CrB candidates, based on the analysis of MACHO optical light curves (Wood & Cohen 2001). Optical Gravitational Lensing Experiment (OGLE) light curves and follow-up optical spectroscopic studies confirm the R CrB status of MSX LMC 439 but optical spectroscopic confirmation was not obtained for MSX LMC 1795 (Soszyński et al. 2009; Tisserand et al. 2009). The optical spectrum of MSX LMC 1795, discussed in Appendix C, confirms that it is an R CrB star. The *Spitzer* spectra of these two stars are shown in Fig. 8. The spectra, representing emission from circumstellar dust, are almost featureless with a very weak peak at 8–9 μm, like those of Galactic R CrB stars (Clayton et al. 2011; Lambert et al. 2001).

3.7 YSOs/H II regions

Fig. 9 shows the spectra of these objects, which are not evolved stars. The spectrum of J053941−692916 shows CO_2 ice at 15.2 μm, and the 4 μm CO_2 ice band was also reported before (Shimonishi et al. 2010), indicating that this object is a YSO (Furlan et al. 2006;

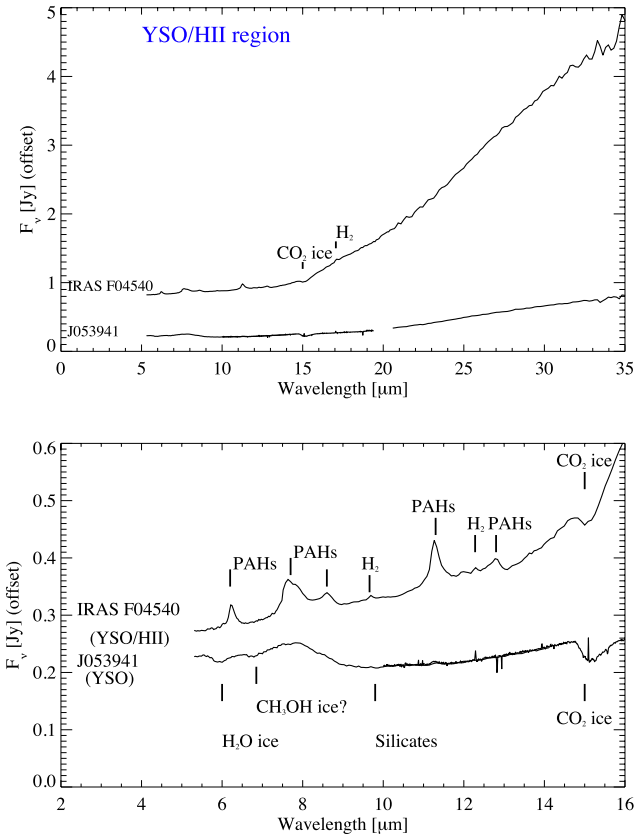

Figure 9. Spectra of the YSO and the H II region observed in the LMC. The spectral region between 6 and 16 μm is enlarged in the lower panel.

Oliveira et al. 2009). Its rising SED up to 35 μm (Fig. 1) is also consistent with the known properties of a YSO. The IR spectrum and the SED resemble those of YSOs of Type-I (Furlan et al. 2008). The absorption at ∼6.8 μm is probably associated with a CH_3OH ice band.

The *Spitzer* spectrum of IRAS F04540−6721 shows CO_2 ice at 15.2 μm (Fig. 9), but it also shows additional PAHs and H_2 emission. The optical spectrum (Fig. C2) shows hydrogen recombination lines, so there is ionization. The object appears to be a YSO, surrounded by a compact H II region. We classify this object as a YSO/H II region.

4 COLOUR–COLOUR AND COLOUR–MAGNITUDE DIAGRAMS

IR colour–colour diagrams and colour–magnitude diagrams have been used to classify objects detected by photometric surveys (e.g. Blum et al. 2006; Matsuura et al. 2009). Such diagrams were also used to find post-AGB star candidates (e.g. van Aarle et al. 2011). As we used IR colours as one of the primary methods to select post-AGB candidates, we re-visit the post-AGB selection criteria on colour–colour and colour–magnitude diagrams.

We used five different types of colour–colour and colour–magnitude diagrams for the selection of the targets; we present one diagram in the main text, while the remaining diagrams are presented in Appendix A. Overall these diagrams can find post-AGB candidates, but there is some contamination by other types of objects which have similar colours.

For comparison with the IR colours of post-AGB stars and other types of objects, we incorporated existing spectroscopically known objects. The sample assembled by Matsuura et al. (2009) is used, containing carbon-rich and oxygen-rich AGB stars and red supergiants (RSGs) from the following sources: Kontizas et al. (2001), Cioni et al. (2001), Sanduleak & Philip (1977), Blanco, Blanco & McCarthy (1980), Westerlund, Olander & Hedin (1981), Wood, Bessell & Fox (1983), Wood, Bessell & Paltoglou (1985), Hughes (1989) and Reid, Glass & Catchpole (1988). We further added samples of AGB stars, post-AGB stars, R CrB stars and PNe from the SAGE-Spec project (Kemper et al. 2010; Woods et al. 2011). Additionally, we assembled S Dor variables, a variety of the LBVs from Van Genderen (2001), Wolf Rayet (WR) stars from Breysacher, Azzopardi & Testor (1999) and post-AGB stars from Gielen et al. (2009). We removed probable galaxies prior to the analysis, following the colour selection used by Matsuura, Woods & Owen (2013). We extracted photometric data from the *Spitzer*-SAGE LMC survey (Meixner et al. 2006), which included near-IR photometry from 2MASS (Skrutskie et al. 2006).

4.1 Colour–colour diagram K–[8.0] versus K–[24]

Fig. 10 shows the colour–colour diagram of K–[8.0] and K–[24], which can be used to find post-AGB candidates. The diagram contains slightly revised boundaries of regions from Matsuura et al. (2013). Oxygen-rich post-AGB stars are found mainly in region (c), with some in the redder part of region (b), whereas carbon-rich post-AGB stars are found in region (d). In Fig. 10, carbon-rich post-AGB stars are separated from carbon-rich AGB stars, because PAH features increase the [8.0]-band fluxes in carbon-rich post AGB stars. Although the sample is small, there is an oxygen-rich AGB star and an oxygen-rich post-AGB star in region (d), as well as YSOs. Oxygen-rich post-AGB stars are mixed with high mass-loss rate oxygen-rich AGB stars in region (c).

5 ANALYSIS OF PAH FEATURES

The primary aim of our *Spitzer* observing programme was to investigate carbon-rich chemistry in LMC post-AGB stars. More specifically, we aimed to understand if the shapes of PAH features would change along the path of stellar evolution from the AGB through the post-AGB to the planetary nebula phases, and if the low metallicity of the LMC has any impact on the PAH features.

In order to increase the sample size, we added spectra of post-AGB stars that were observed by other *Spitzer* programmes, as was done in our previous paper (Volk et al. 2011). The collected data are summarized in Table 2. The data were assembled from programmes, proposal ID 30788 (PI: Sahai) and proposal ID 40159 (project name, SAGE-Spec; Kemper et al. 2010). As a part of SAGE-Spec, all LMC archival spectra were reduced and provided as a data product, we use these reduced data for this additional sample; the data reduction process was described by Kemper et al. (2010). Additionally, we included the H II region IRAS F04540−6721 and the PN SMP LMC 75 from our *Spitzer* programme in the PAH analysis, as both of them showed PAHs.

5.1 Continuum subtraction

In order to examine intrinsic profiles of PAH features, we subtracted the continua from the observed spectra. We estimated the continuum level by spline fits through the five intervals (5.8–5.9, 6.8–7.0, 9.2–9.4, 9.8–10.2 and 14.3–15 μm). Some examples of continua are presented in Fig. 11. In addition, following Peeters et al.'s analysis of 6–9 μm features, we set local continua between 6 and 9 μm on the spectra (Fig. 11) for class $\mathcal{A}$ and class $\mathcal{B}$, where classes will

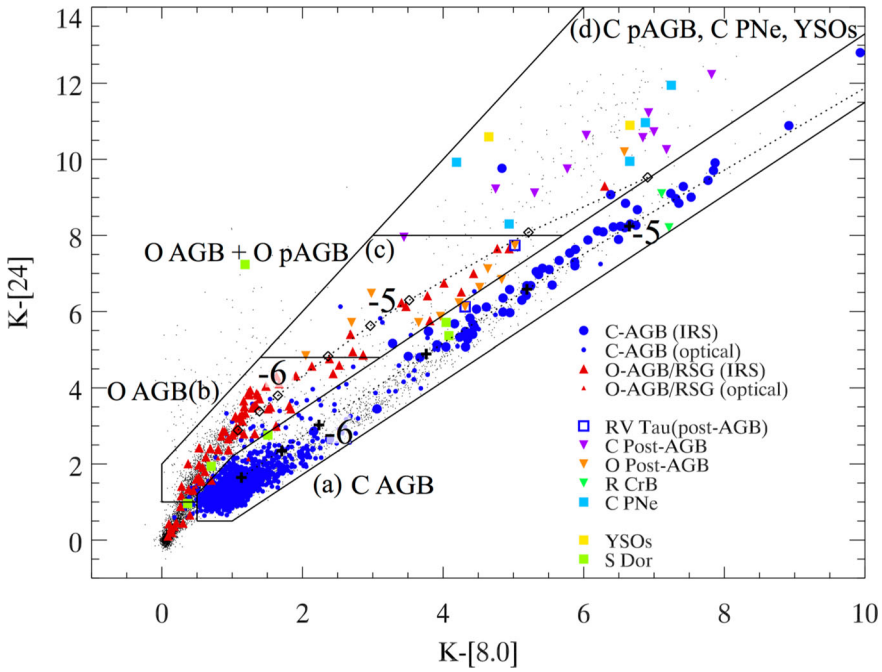

Figure 10. The Ks–[8.0] versus Ks–[24] colour–colour diagram of the LMC objects. The black dots show all of the data in the SAGE data base, combined with 2MASS photometric data. Other symbols show the sources with known spectral classifications. C-AGB: carbon-rich AGB stars, where 'IRS' represents objects classified from *Spitzer* IRS observations, and 'optical' represents objects classified on the basis of optical spectra. O-AGB: oxygen-rich AGB stars, RV Tau: RV Tauri stars, C post-AGB: carbon-rich post-AGB stars, O post-AGB: oxygen-rich post-AGB stars, R CrB: R CrB stars, C PNe: carbon-rich PNe. The boxes highlight the object types typically found in the colour ranges indicated. Carbon-rich post-AGB stars are found in region (d) and are well separated from carbon-rich AGB stars, but region (d) also contains PNe and YSOs. Oxygen-rich post-AGB stars are found in region (c). The two dotted lines show the typical colour at a given mass-loss rate of oxygen-rich (diamonds) and carbon-rich (plus signs) AGB stars. The diamond and plus sign symbols show the mass-loss rates 3×10^{-7}, 6×10^{-7}, 1×10^{-6}, 3×10^{-6}, 6×10^{-6}, 1×10^{-5}, 3×10^{-5} and 6×10^{-5} $M_{\odot}$ yr^{-1}, and the colours for 1×10^{-6} and 1×10^{-5} $M_{\odot}$ yr^{-1} are indicated with -6 and -5.

Table 2. List of carbon-rich post-AGB stars used for PAH analysis.

No.	Names	SAGE Coordinates (J2000)	Programme ID	Spt.	PAHs				
					6–9 μm Overall[a]	6.2	7.7[b]	8.6[b]	11–14 μm
2	IRAS F04540−6721	04 54 03.62 −67 16 18.2	50338	(YSO/H II)	$\mathcal{A}$	(A	A′	A″)	α
	IRAS 05063−6908	05 06 03.67 −69 03 58.8	30788		$\mathcal{D}$	(D?	D?)		δ
	IRAS 05073−6752	05 07 13.91 −67 48 46.6	40159		$\mathcal{D}$	(D	D)		β
8	IRAS 05092−7121	05 08 35.94 −71 17 30.5	50338	late B- early G	$\mathcal{B}$	(B	B′	A″)	β
9	IRAS 05110−6616	05 11 10.61 −66 12 53.8	50338	F3II(e)	$\mathcal{D}$	(D	D)		γ
	IRAS 05127−6911	05 12 28.18 −69 07 55.7	40159		$\mathcal{A}$	(B?	A′?	A″)	(noisy)
	IRAS F05192−7008	05 18 45.26 −70 05 34.5	40159		$\mathcal{B}$?	(B?	B′?	?)	γ
	IRAS 05185−6806	05 18 28.17 −68 04 04.1	30788		$\mathcal{B}$	(B	B′	B″)	β
11	J052043.58−692341.4	05 20 43.58 −69 23 41.4	50338	F5Ib(e)	$\mathcal{D}$	(D	D)		γ
14	2MASS J05252077−7050075	05 25 20.75 −70 50 07.3	50338	A1Ia/F2-F5I	$\mathcal{D}$	(D	D)		γ
18	SMP LMC 75	05 33 46.96 −68 36 44.1	50338	(PN)	$\mathcal{B}$	(B	B′	B″)	α
	IRAS 05360−7121	05 35 25.84 −71 19 56.7	30788		$\mathcal{B}$	(B	B′	B″)	β
	IRAS 05370−7019	05 36 32.52 −70 17 38.4	40159		$\mathcal{A}$?	(B?	A′?	B″?)	δ
	IRAS 05537−7015	05 53 11.96 −70 15 22.6	40159		$\mathcal{A}$	(B?	A′?	A″?)	δ
24	IRAS 05588−6944	05 58 25.94 −69 44 25.7	50338	WC?	$\mathcal{A}$	(A	A′	A″)	β

[a]The primary classification of the PAH features at 6–9 μm, considering three features at 6.2, 7.7 and 8.6 μm. The *Spitzer* spectrum of IRAS 05370−7019 is noisy and it is difficult to determine the PAH classifications.
[b]For class D, there is one broad peak between 7 and 9 μm rather than two distinct features at 7.7 and 8.6 μm.

be discussed later. This further subtraction of local continua makes it easier to examine the features at 7–9 μm. For 10–14 μm, we did not set any local continuum, so that a 'plateau', as described by Peeters et al. (2004), is included in our PAH spectral analysis if it is present.

5.2 Features at 6–9 μm

Fig. 12 shows the 6–9 μm continuum-subtracted spectra of 13 post-AGB stars, one PN and one YSO/H II region in the LMC. Two or three features were found at ∼6.3, 7.6–8 and 8.6 μm, which are associated with PAHs.

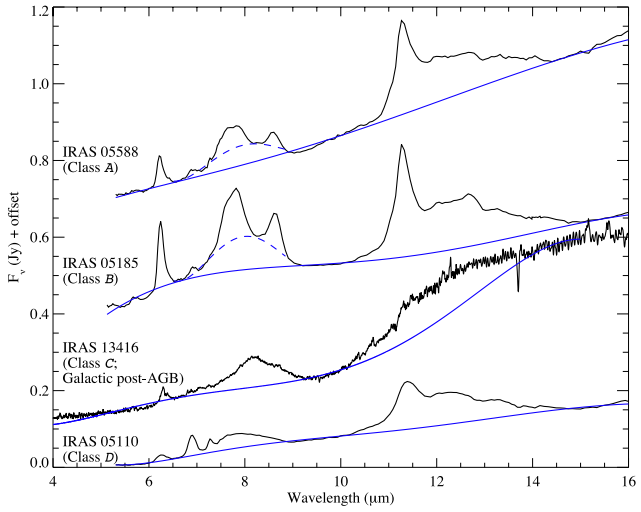

Figure 11. Examples of the continua (blue lines), which were subtracted from the observed spectra, in order to emphasize the intrinsic PAH spectra. The local continua at 6.5–9 μm are indicated by dashed lines.

Peeters et al. (2002) examined the shapes of the features in the 6–8 μm region and divided the spectra into three classes according to the peak positions of the feature: $\mathcal{A}$, $\mathcal{B}$ and $\mathcal{C}$. The templates of these profiles from Peeters et al. (2002) are also plotted in Fig. 12. These templates were taken with the *ISO*/SWS, which had the spectral resolution of $R = \lambda/\Delta\lambda$=500–1500, and were smoothed with the *Spitzer* IRS spectral resolution.

In addition to broad features that are widely recognized as PAHs, there are features at ∼6.9 and 7.3 μm in some of the post-AGB stars (Fig. 12). Although the assignments of these two features are still debated (Tielens 2008), they are most likely attributed to aliphatic carbons (Duley & Williams 1981; Kwok, Volk & Bernath 2001).

5.2.1 *Class* $\mathcal{A}$

According to Peeters et al.'s scheme, class $\mathcal{A}$ profile is characterized by peaks located at ∼6.22, 7.6 and ∼8.6 μm, which correspond to subclasses A, A′ and A″, respectively. There is a secondary peak at about 7.8 μm on the shoulder of the 7.6 μm feature, but the 7.8 μm peak is weaker than the 7.6 μm peak. The subclasses

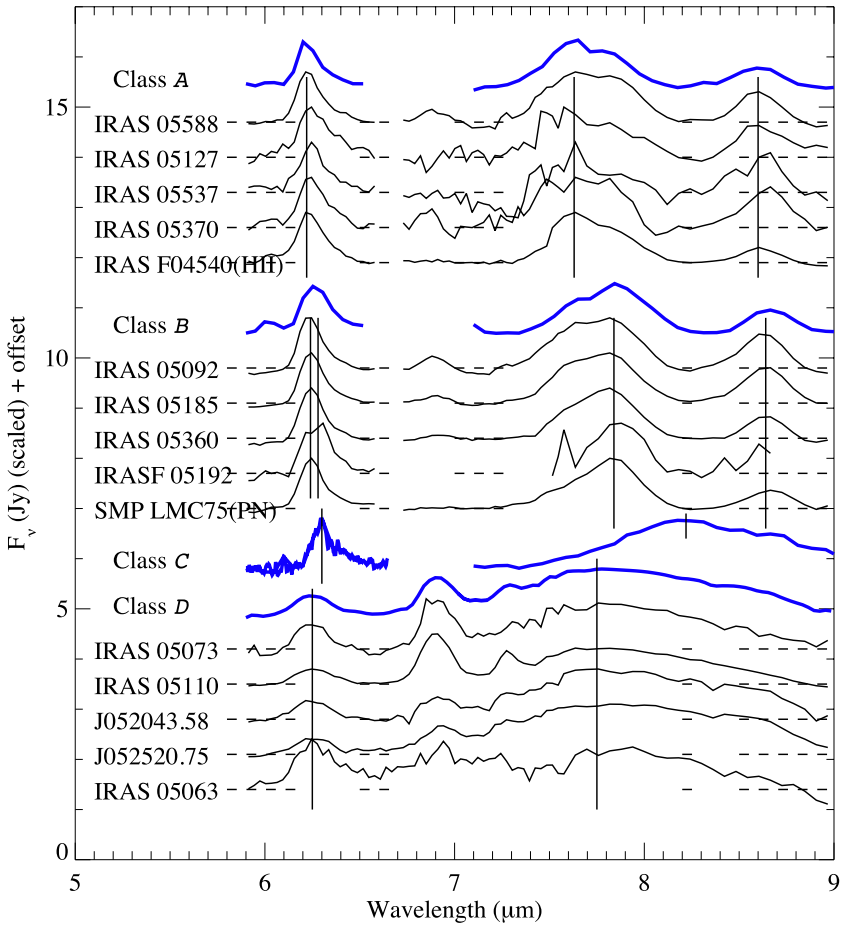

Figure 12. Continuum-subtracted *Spitzer* spectra at 6–9 μm for C-rich post-AGB stars and two other objects in the LMC listed in Table 2. Templates of the class $\mathcal{A}$, $\mathcal{B}$ and $\mathcal{C}$ PAH profiles (Peeters et al. 2002) are plotted as bold lines, and PAH spectra of LMC post-AGB stars which match these classes follow below. Spectra of five LMC post-AGB stars do not match any previously known PAH profiles, and we name these as class $\mathcal{D}$. The average of these five class $\mathcal{D}$ spectra is plotted as the bold line. All of the spectra are scaled, and the 'continuum' levels are marked with dashed lines. Vertical lines indicate the peak wavelengths of PAH features.

(A, A′, A″) generally correspond to the major class $\mathcal{A}$ but some objects have slightly different subclasses from the major class (Peeters et al. 2002).

The expected peak wavelengths of the profiles are marked with vertical lines in Fig. 12. Amongst our sample, five objects have profiles matching the class $\mathcal{A}$ profile: four post-AGB stars, IRAS 05588−6944, IRAS 05127−6911, IRAS 05370−7019, IRAS 05537−7015 and the H II region IRAS F04540−6721. Three objects (IRAS 05127−6911, IRAS 05370−7019 and IRAS 05537−7015) have noisy spectra, and we classified these three as class $\mathcal{A}$ based on their features having approximate peaks at about 7.6 μm, but the peak at ∼6.2 μm might suggest that these could be placed in class $\mathcal{B}$.

Peeters et al. (2002) demonstrated that the class $\mathcal{A}$ profile was found usually in objects heated by hot stars, whose spectral types are O–B. Objects with the class $\mathcal{A}$ profile included H II regions and post-AGB stars. Indeed, the H II region in our sample has a class $\mathcal{A}$ profile, which is consistent with Peeters et al.'s finding.

5.2.2 Class $\mathcal{B}$

The class $\mathcal{B}$ profile differs from that of class $\mathcal{A}$ by having the peaks of the three features shifted towards longer wavelength. The peaks are found at about ∼6.24–6.28, 7.8–8.0 and >8.62 μm, which have been assigned the subclasses B, B′ and B″ (Peeters et al. 2002). Subclass B had a slightly wider feature around 6.2 μm than subclass A.

Five objects have a class $\mathcal{B}$ (Fig. 12) PAH profile: four post-AGB stars (IRAS 05092−7121, IRAS 05185−6806, IRAS 05360−7121 and IRAS F05192−7008) and one PN (SMP LMC 75). All of these objects have the class B′ feature peaking at about 7.8 μm and the class B feature peaking at about 6.24 μm. The spectrum of IRAS F05192−7008 is noisy, but it seems to have three peaks corresponding to class $\mathcal{B}$.

Peeters et al. (2002) found that objects with the class $\mathcal{B}$ profiles included PNe and post-AGB stars. We found that the PN, SMP LMC 75 is class $\mathcal{B}$, which is consistent with what has been found for Galactic, and later for Magellanic Clouds PNe (Bernard-Salas et al. 2009).

5.2.3 Class $\mathcal{C}$

Peeters et al. (2002) characterized class $\mathcal{C}$ spectra as having a peak at 6.3 μm and a broad feature from 7.5 to 9.3 μm, whose peak is located at 8.22 μm (Fig. 12). Unlike classes $\mathcal{A}$ and $\mathcal{B}$, which have two separate features in the wavelength range of 7.5–9.3 μm, class $\mathcal{C}$ has a single broad feature.

Peeters et al. (2002) had a sample of 57 objects, but only two were assigned to class $\mathcal{C}$, both of which were post-AGB stars. Later, more class $\mathcal{C}$ objects were found, including T Tauri stars and Herbig Ae and Be stars (Keller et al. 2008).

In our sample, we did not find any objects matching the criteria of class $\mathcal{C}$, with a broad feature peaking at about 8.22 μm. Five objects in our LMC post-AGB sample show a similar profile to that of class $\mathcal{C}$ but the peak wavelength falls at a much shorter wavelength of about 7.7 μm. In addition, their 6.25 μm features are broader than those found in the Galactic class $\mathcal{C}$ objects, and the peak is at 6.2 μm, shorter than the ∼6.3 μm for class $\mathcal{C}$. These five LMC objects are different from class $\mathcal{C}$, and we call their profile class $\mathcal{D}$.

The shift of the 8.2 μm peak to 7.7 μm is intrinsic to the object, and is not an artefact of the continuum subtraction. Fig. 11 shows the observed spectra, including the example of IRAS 05110−6616 (class $\mathcal{D}$) and IRAS 13416−6243 (Galactic post-AGB star, class $\mathcal{C}$). The difference in the peak wavelength of the broad feature was already found in the observed spectra. This is further discussed in Appendix B.

5.2.4 Class $\mathcal{D}$

The five objects, mentioned above, which do not fit into the existing classes $\mathcal{A}$–$\mathcal{C}$, are taken as the prototypes of a new class $\mathcal{D}$. Class $\mathcal{D}$ is characterized by a broader feature peaking at 6.24 μm, and a broad single feature from 7–9 μm, peaking at about 7.7 μm. The peak wavelengths are shifted shortwards, compared with class $\mathcal{C}$. In Fig. 12, five class $\mathcal{D}$ objects are plotted, and the average of these five class $\mathcal{D}$ profiles is plotted as a bold line.

Class $\mathcal{D}$ has some additional differences from classes $\mathcal{A}$ and $\mathcal{B}$. At 6.0 μm, the class $\mathcal{A}$ and $\mathcal{B}$ templates have a small secondary peak next to the 6.2 μm feature, but this feature is not apparent in the class $\mathcal{D}$ spectra.

All five class $\mathcal{D}$ objects in our LMC sample show an additional feature at 6.9 μm. This feature is not found or is weak in the class $\mathcal{A}$ and $\mathcal{B}$ objects in our sample: only a hint of this feature is found in IRAS 05092−7121 and IRAS 05185−6806. Note that the templates from Peeters et al. (2002) focused on the 6.3 and 7.2–9 μm features, which are associated with PAHs, so that this 6.9 μm feature was not included in these templates (Fig. 12). The spectrum of the PN NGC 7027, which is of class $\mathcal{B}$, shows the 6.9 μm feature. The origin of the 6.9 μm feature is probably aliphatic carbon, but this has not been well established.

Among five class $\mathcal{D}$ objects in our sample, three stars (IRAS 05110−6616, J052043.58−692341.4 and 2MASS J052520.77−705007.5) have the 21 μm feature and the other two (IRAS 05063−6908 and IRAS 05073−6752) also have a hint of the 21 μm feature (Volk et al. 2011). The class $\mathcal{D}$ and the 21 μm feature may be of similar origin.

Peeters et al. (2002) have pointed out that IRAS 22272+5435 and IRAS 07134+1005 show a broad single feature at ∼8 μm similar to the class $\mathcal{C}$ profile, but its peak was shortwards of the class $\mathcal{C}$ 8.22 μm peak. They did not include those two objects in class $\mathcal{C}$. We classify these two stars as class $\mathcal{D}$ (Fig. 13). Additionally, IRAS 05341+0852 might potentially have the class $\mathcal{D}$ feature, though its spectrum is too noisy to confirm this. We searched for additional post-AGB spectra in the *ISO*/SWS archive (http://irsa.ipac.caltech.edu/data/SWS/) and data collected by Sloan et al. (2003). We found that two Galactic post-AGB stars (IRAS 04296+3429 and IRAS 22574+6609) have a profile intermediate between those of classes $\mathcal{C}$ and $\mathcal{D}$.

All the class $\mathcal{D}$ objects with known spectral types have a central star of type F or G (Tables 2 and 3). It is possible that spectral types of the central stars and PAH profiles are correlated.

5.3 PAHs at 10–14 μm

The 10–14 μm spectra of PAHs have been used as diagnostics for PAH substitution patterns (e.g. Socrates 2001). Fig. 14 shows the continuum-subtracted 10–17 μm spectra of 14 objects in our sample. The spectrum of IRAS 05127−6911 was excluded, because it is too noisy in this wavelength range.

We grouped the PAH 10–14 μm profiles into four classes α–δ, based on the peak wavelengths and the shapes of the subfeatures. The characters of these classes are described in the following subsections, and the assigned classifications are summarized in Table 2.

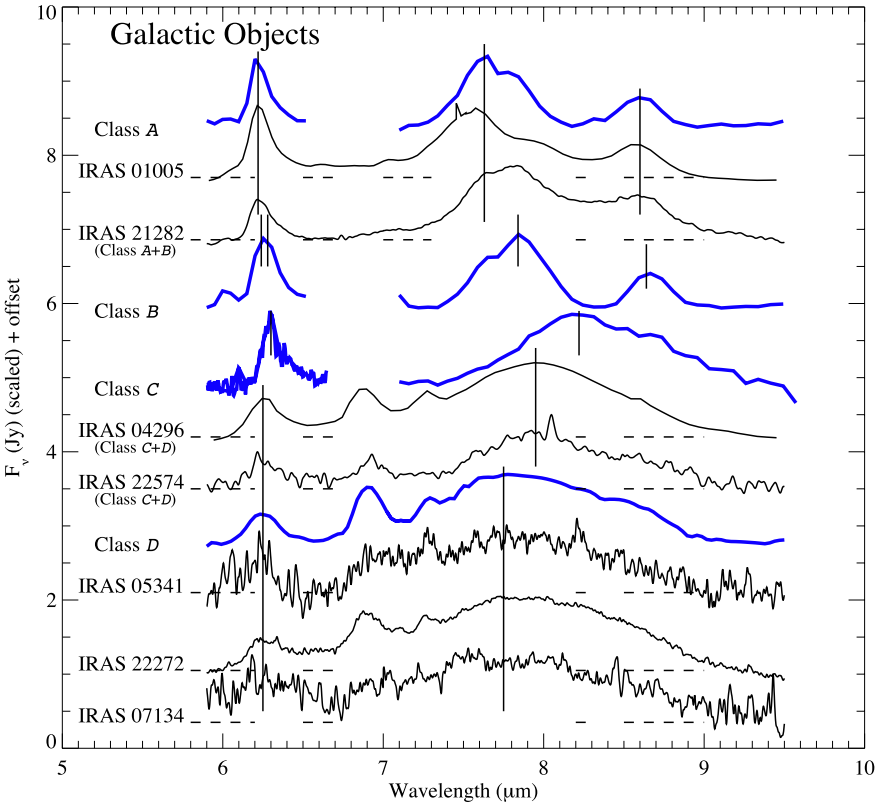

Figure 13. Continuum-subtracted spectra of representative Galactic post-AGB stars, showing the differences in the 6–9 μm spectra. Template spectra of the classes $\mathcal{A}$–$\mathcal{C}$ and the average of the LMC class $\mathcal{D}$ profile are plotted. The spectra of the Galactic post-AGB stars, IRAS 04296+3429 and IRAS 22574+6609 show a profile between the classes $\mathcal{C}$ and $\mathcal{D}$, with a 7.5–9 μm broad feature peaked at about 7.9 μm. IRAS 05341+0852 and IRAS 22272+5435 show the class $\mathcal{D}$ profile. IRAS 22272+5435 has an additional unidentified feature at 6.35 μm.

Table 3. List of carbon-rich post-AGB stars in Fig. 13.

Name	PAHs		Sp. or $T_{\rm eff}$	Ref.
	6–9 μm	10–14 μm		
IRAS 01005+7910 A		β	$T_{\rm eff} = 21\,500$ K	Hrivnak et al. (2000), Klochkova et al. (2002), Zhang, Kwok & Hrivnak (2010)
IRAS 04296+3429 C+D			G0I, F3I, $T_{\rm eff} = 7\,000$ K	Bakker et al. (1997), Klochkova et al. (1999), Van Winckel & Reyniers (2000), Volk et al. (2002), Sánchez Contreras et al. (2008)
IRAS 05341+0852 D			G2Ia, F5I, $T_{\rm eff} = 6\,500$ K	Bakker et al. (1997), Hrivnak et al. (2000), Van Winckel & Reyniers (2000) Suárez et al. (2006)
IRAS 07134+1005 D			F5I, $T_{\rm eff} = 7\,250$ K	Hrivnak, Kwok & Volk (1989), Hrivnak et al. (2000), Van Winckel & Reyniers (2000)
IRAS 13416−6243 C			G1I	Hu et al. (1993), Peeters et al. (2002)
IRAS 21282+5050 A+B		δ+?	Of7-[WC 11]	Cohen & Jones (1987)
IRAS 22272+5435 D		unclassified	G5Ia,, $T_{\rm eff} = 6\,500$ K	Kwok, Hrivnak & Geballe (1994), Hrivnak et al. (2000), Van Winckel & Reyniers (2000)
IRAS 22574+6609 C+D			A1–6I	Hrivnak et al. (2000), Sánchez Contreras et al. (2008)

For comparison, we included the classifications of the 6–8 μm PAH features next to the object names in Fig. 14. There is no correlation between the classifications at 10–14 μm and 6–9 μm.

Previously, van Diedenhoven et al. (2004) classified the PAH profiles at 11.2 μm into three categories $A_{11.2}$, $A(B)_{11.2}$ and $B_{11.2}$, as part of an overall PAH classification of 3–12 μm spectra. However, because we found that the spectra at two different wavelength ranges of 10–14 μm and 6–9 μm are not correlated, we set up a separate classification scheme for 10–14 μm. We specifically use large math characters to classify the 6–9 μm features and use $\mathcal{A}$ and $\mathcal{B}$ for the ∼6.2 μm feature only, and we use Greek letters for 10–14 μm. van Diedenhoven et al.'s $A_{11.2}$ and $B_{11.2}$ categories relate to the 11.2 μm feature only; the distinction is that the peak wavelength falls at 11.2–11.24 and 11.25 μm, respectively, with full widths at half-maximum (FWHMs) of 0.17 and 0.21, respectively. We concluded that these characters fit our classes α and β, respectively, as defined below. van Diedenhoven et al.'s third class, $A(B)_{11.2}$ has a feature at the same peak wavelength as $A_{11.2}$, but its width (∼0.21 μm in FWHM) is slightly greater than that of class $A_{11.2}$, ∼0.17 μm in FWHM. $B_{11.2}$ and $A(B)_{11.2}$ can be distinguished with *ISO*/SWS spectra, which has a resolution ($\lambda/\Delta\lambda$) over 1000, but is hard to do so with the *Spitzer* IRS resolution (68–128). We do not set a classification equivalent to Class $A(B)_{11.2}$.

5.3.1 *Class α*

The class α is characterized by a sharp 11.3 μm feature, together with a well-isolated 12.7 μm feature (Fig. 14). There is an additional

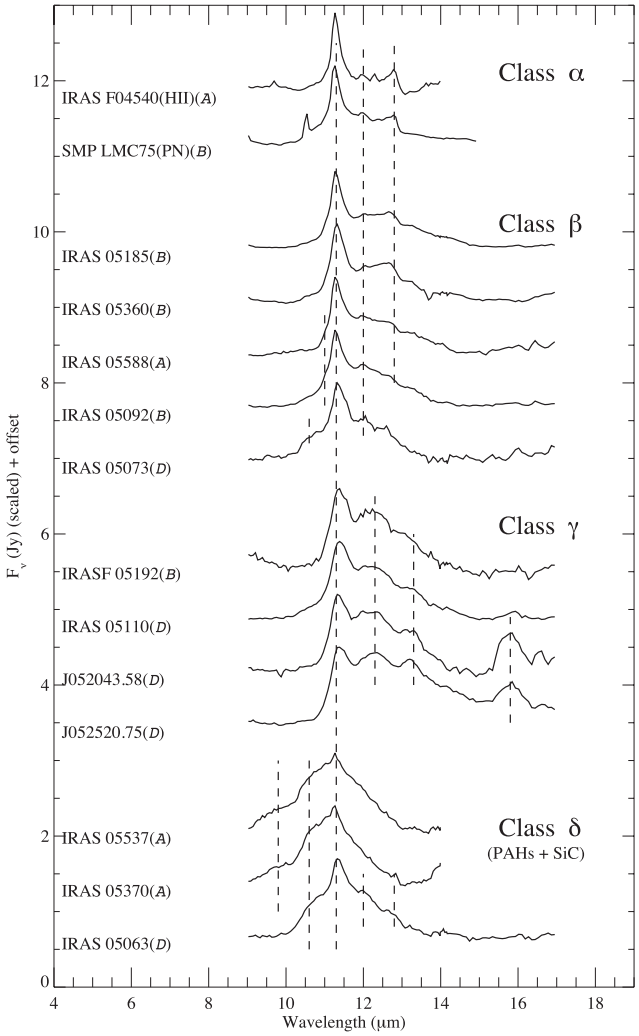

Figure 14. Continuum-subtracted *Spitzer* spectra at 9–17 μm for C-rich post-AGB stars and two others in the LMC, from Table 2. The spectra are classified into four categories α–δ based on the PAH features at 10–14 μm. The class α–γ spectra are associated with PAHs, while the class δ profile is composed of PAHs and SiC. Object names are indicated on the left, followed by the 6–8 μm PAH classes ($\mathcal{A}-\mathcal{D}$).

feature at 12.0 μm, but it is very weak. The 11.3 μm feature is the strongest among these three features, though in the Galactic sample, some objects have the 12.7 μm feature as strong as the 11.3 μm one (Hony et al. 2001). The combination of these three distinct features is typically found in PNe such as the Galactic PN NGC 7027 (Hony et al. 2001). In our sample, an H II region and a PN have this class.

5.3.2 *Class β*

The class β profile shows a slight difference from the class α (Fig. 15). The 11.3 μm feature is wider, and the long wavelength edge of the feature declines much more gradually than in class α. The 12.7 μm feature declines more gradually towards longer wavelength than in class α. The long wavelength tail of the 11–12 μm complex can continue up to 14 μm. The feature at 12.0 μm is also found but is often weak. Among our LMC post-AGB sample, five objects have this type of profile, as does one Galactic post-AGB star (Fig. 16).

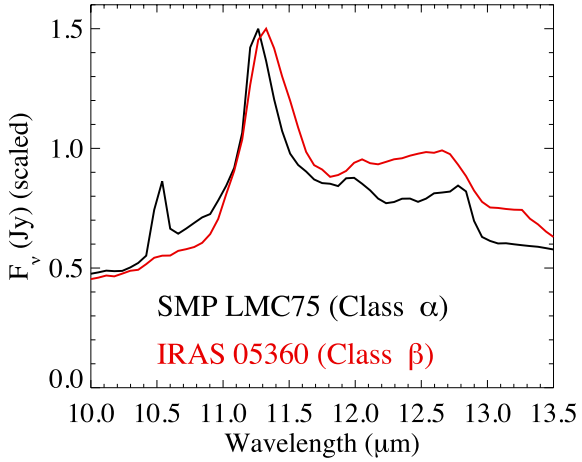

Figure 15. Comparison between class α and β features at PAH 10–14 μm. Class β has a wider 11.3 μm feature, with a peak at longer wavelength, and the 12.7 μm feature declines more gradually than in class α.

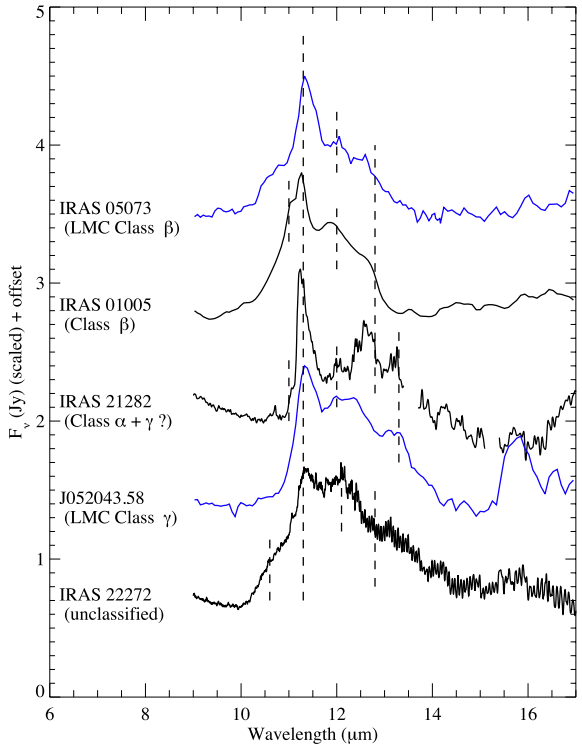

Figure 16. The 9–16 μm continuum-subtracted spectra of Galactic post-AGB stars, whose 6–9 μm spectra are shown in Fig. 13. Only spectra of good quality are plotted. The PAH classifications are indicated below the object names. The spectrum of IRAS 22272+5435 does not match any of the classes, but possible SiC at 10.8 μm suggests class δ with some contribution of PAHs at 13 μm as found in class γ object. Kwok et al. (2001) proposed that the 9–16 μm spectrum of IRAS 22272 might contain aliphatic carbon features, making this spectrum unique.

There is a very weak feature at 11.0 μm on the shoulder of the 11.3 μm bands in two objects (IRAS 05588−6944 and IRAS 05092−7121). This 11.0 μm feature is also associated with PAHs (van Diedenhoven et al. 2004; Tielens 2008). IRAS 05073 has a hint of SiC contribution, which is found in class δ objects.

5.3.3 Class γ

Spectra with broad triple features at 11.3, ∼12.3 and ∼13.3 μm are classified as γ. These features are broad and connected, rather than being two distinct features at 11.3 and 12.7 μm as found in the class α and β objects. The combination of features can sometimes extend to nearly 15 μm, as found in 2MASS J05252077−7050075 (Fig. 4). Among our post-AGB sample, four objects have this profile.

Two of the class γ objects have a feature at 15.8 μm (J052043.58−692341.4 and 2MASS J05252077−7050075). Its assignment has been suggested to be carbonaceous molecules or dust (Hrivnak et al. 2009; Volk et al. 2011). There are PAH features at 15.8 μm (Socrates 2001; Moutou, Leger & D'Hendecourt 1996; Van Kerckhoven et al. 2000); however, Hrivnak et al. (2009) pointed out that the features found in post-AGB stars were wider (∼1.3 μm) than the PAH features found in H II regions, PNe and Herbig AeBe stars. C_{70} has a feature at this wavelength as well (Cami et al. 2010), but lack of other C_{70} associated features at 17.5 and 18.7 μm eliminates this possibility. The 15.8 μm feature is probably associated with PAH ring deformation vibrations (Socrates 2001), but additional contributions should be considered.

5.3.4 Class δ

The remaining three objects are classified as class δ. They have a very broad feature extending from 10 to 14 μm (Fig. 14), with a sharp PAH feature at 11.3 μm on top. There is an additional weak feature at 10.8 μm on the short-wavelength shoulder of the 11.3 μm feature. The broad feature and the 10.8 μm feature are associated with SiC, which we will discuss in the following section. There is a broad secondary feature at 9.8 μm, but its identification is unknown.

5.4 Continuum and features

Fig. 17 shows comparison of the overall PAHs and SEDs of the LMC post-AGB star, IRAS F05110−6616 and two Galactic post-AGB stars, IRAS 05341+0852 and IRAS 22272+5435. All three post-AGB stars have, or likely to have $\mathcal{D}$ PAH feature at 6–9 μm, IRAS F05110−6616 and IRAS 05341+0852 have similar spectra in this wavelength range, including the continuum levels. In contrast, a difference of these two spectra is found at 10–14 μm PAH features. The difference at 10–14 μm but similarities at 6–9 μm PAHs and continuum suggest that either compositions or bonding structures of PAHs that emit at two different wavelength range differ.

6 FITS WITH EXPERIMENTAL PAH CROSS-SECTIONS

6.1 Methods

We attempt to fit *Spitzer* spectra with laboratory-measured PAH cross-sections to test whether they, especially those of the new class γ, do indeed show the presence of PAHs. The features at 10–14 μm were used to diagnose the structure of aromatic rings (Socrates 2001) and we focus on this wavelength region, which was extensively studied in the laboratory (e.g. Hudgins & Sandford 1998).

We fitted the *Spitzer* continuum-subtracted spectra at 10–14 μm with a composite of the NASA Ames laboratory spectra (Bauschlicher et al. 2010; Mattioda et al., in preparation). The NASA Ames data base contains theoretical and experimental cross-sections, and we use the experimental cross-sections, as they have higher accuracy in the wavelengths of the features. We focused

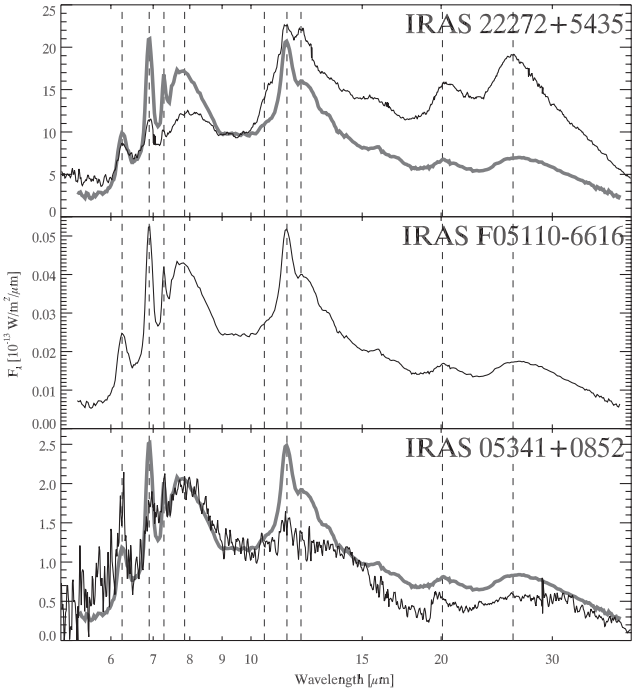

Figure 17. Comparison of the spectra of the LMC post-AGB star, IRAS F05110−6616 with two Galactic post-AGB stars, IRAS 05341+0852 and IRAS 22272+5435. The top and middle panel, the spectrum of IRAS F05110−6616 is plotted in grey colour for comparison, with the flux scaled at 9.0–9.6 μm.

on PAHs consisting of carbon and hydrogen only, though the data base includes PAHs containing nitrogen, oxygen and silicon. That resulted in 40 laboratory spectra, consisting of 30 neutral and 10 ionized PAH compounds. The smallest PAH compound used in the analysis was $C_{14}H_{10}$ (phenanthrene and anthracene) and the largest one was $C_{50}H_{22}$. The largest ionized compound was $C_{24}H_{12}^{+}$ (coronene). The laboratory spectra were convolved with the Lorentzian line profile, and further smoothed to the *Spitzer* spectral resolution. We tested the fits by minimizing χ^2. We convolved the laboratory cross-section with a blackbody. In the small spectral range of 10–14 μm, the spectral gradient caused by the temperature variation was small. 'Redshift' in the laboratory data (Mattioda et al., in preparation) is ignored, as this shift is smaller than the *Spitzer* spectral resolution. Some *Spitzer* spectra showed a trace of the SiC band at 11.3 μm, so we included the SiC feature as well as PAHs in our χ^2 fitting process. We extracted 10–15 μm *ISO*/SWS spectra of the Galactic carbon star, W Ori (Sloan et al. 2003), as a SiC template.

The spectrum of the PN, SMP LMC 75, has an [S IV] emission line at 10.6 μm and possibly the [Ne II] line at 12.8 μm. We masked the 10.6 μm region, but included the 12.8 μm region, as the latter line was insignificant.

We attempted unsuccessfully to fit 6–9 μm spectra in the same way. This was partly hampered by the limitations of the χ^2-minimization fitting method. The χ^2-fitting tends to capture the global trend of the features, but sometimes has difficulty in simultaneously fitting a combination of broad and sharp features as found in observed 6–9 μm spectra. Additionally, post-AGB stars are likely to have both PAHs and aliphatic carbon features at this wavelength range, making it more difficult to fit (e.g. Hrivnak, Volk & Kwok 2000; Kwok & Zhang 2011). An alternative possibility is that nitrogen-substituted PAHs or hydrogenation might be

important in this wavelength range (Tielens 2008; Duley & Williams 1981). We leave the fitting of the 6–9 μm wavelength for future investigations.

6.2 Results of PAH fitting

Fig. 18 shows the fits to the *Spitzer* continuum-subtracted spectra. Generally, a composite of 40 laboratory spectra can reproduce the overall shapes of the observed 10–14 μm spectra.

Spitzer spectra demonstrate the range of spectral variations of PAHs in post-AGB stars, PNe and H II regions. The variation of the 10–14 μm feature is partly reproduced by composite laboratory PAH spectra. The fits demonstrated that these features are predominantly attributable to PAHs, and the variations of features (except for class δ) are due to the different varieties of PAHs. We are particularly interested in the fitted results of the class γ objects, as the peak wavelength differs from those found in classes α and β, and indeed a combination of the PAH laboratory data can reproduce the 11.4 μm peak and the 12 and 13 μm broad features.

We found that some observed features were fitted better in one class than in the other classes. The observed *Spitzer* spectra showed a slight shift in the peak wavelength of the 11.2–11.4 μm feature (Fig. 15). The peak appeared at 11.2–11.3 μm in class α, whereas this was found at 11.4 μm in class γ. The composite laboratory spectra tended to reproduce the 11.4 μm feature well but not as well as the 11.3 μm feature. The class α objects were a PN and an H II region; these have hot central stars, which ionize the surrounding nebulae. Classes β and γ were associated with post-AGB stars, i.e. the central stars are cooler and their circumstellar material tends to be more neutral (Table 2). The poorer fits of the class α objects are probably due to the current limited availability of laboratory data for ionized PAHs. There were spectra for 30 neutral PAHs in the NASA PAH data base, but for only 10 ionized PAHs. This suggests that a future investment in laboratory measurements of ionized PAHs might improve fits to the class α PAHs. Tielens (2008) suggested that the typical size of PAHs are 50 carbon atoms, so that laboratory measurements of larger PAHs will improve the fitting in general.

The class δ objects showed a broad feature centred at about ∼11 μm, with a sharp feature at ∼11.3 μm on top of that. Our fits show that the broad feature is due to SiC, and it dominated the overall shape, accounting for >90 per cent of the energy in the 10–13 μm region. The sharp feature at 11.3 μm is due to PAHs, though the fits are not great. Additionally, though IRAS 05073−6752 was classified as β, its spectrum shows a hint of SiC at a shoulder shortwards of the 11.3 μm feature.

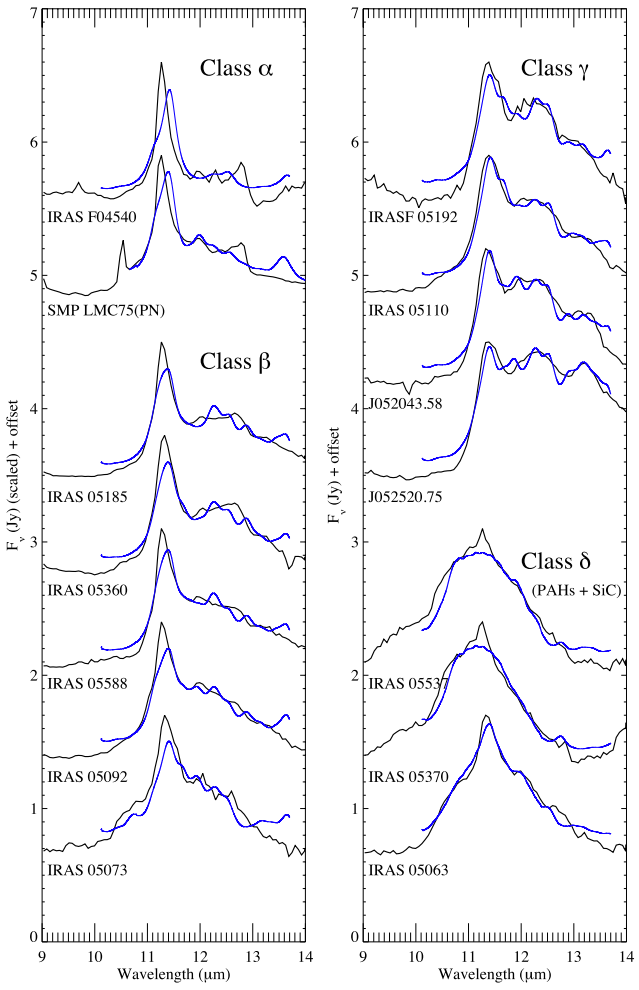

Figure 18. The composite PAH(+SiC) spectra (blue lines), compared with observed *Spitzer* spectra (black lines).

7 DISCUSSIONS AND CONCLUSIONS

Spitzer Space Telescope spectra of the LMC post-AGB stars showed a wide variety of features in mid-IR wavelengths. The class γ type PAH spectra, which have three broad features in the 11–14 μm region, and the class $\mathcal{D}$ spectra, characterized by a broad feature peaking at 7.7 μm, were found in post-AGB objects in the LMC. The PAHs responsible for the γ and $\mathcal{D}$ type spectra tend to be found more in post-AGB stars than in any other types of objects that carry PAHs.

Previous studies of PAHs in Galactic objects have found that the central wavelength of ∼8 μm PAH feature correlates with the effective temperature of the central star (Sloan et al. 2007; Boersma et al. 2008; Smolders et al. 2010). Objects with our newly found class $\mathcal{D}$ PAHs appear to be outliners from this correlation (as found in Fig. 19). In this figure, grey shadow shows the linear fit to the

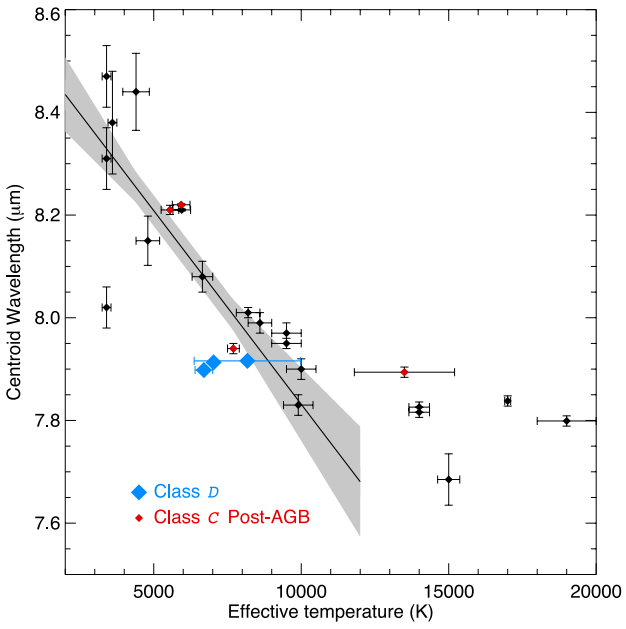

Figure 19. The central wavelength of ∼8 μm PAH feature as a function of the temperature. Class-$\mathcal{D}$

correlation (Smolders et al. 2010), and the spectral types of class $\mathcal{D}$ objects are converted to the effective temperatures (Cox 2000). The previously reported correlation predicts that the stars with effective temperature of 6100–9730 K should show a peak of PAHs at about 8.2 μm. However, these class $\mathcal{D}$ objects have the peak at 7.8–7.9 μm, much shorter than the expected wavelength from the effective temperature. This correlation has been thought to be caused by a change of PAH compositions, as the central stars evolve and their increasing energetic radiation affects the PAHs. Our finding of class $\mathcal{D}$ objects suggest that the compositions of PAHs might be more variable than previously thought.

A wide variety of PAH features have been found in our study, but mainly in the post-AGB stars. By the time the central star evolves into the PN phase, PAHs may have been processed and the profiles changed into class A or B at 6–9 μm and class α at 10–14 μm. PAHs in post-AGB stars and PNe seem to have been altered by UV radiation as the star evolves towards higher surface temperature following the AGB stage, and PAH features change their shape. By the time PAHs are ejected from carbon-rich AGB stars into the ISM, PAHs would already be processed, and spectral characteristics would not differ so much from what is found in the ISM.

The question remains why low metallicity impacts on the profiles of PAHs emitted from the ISM of galaxies (Draine et al. 2007), although little difference has been found in PAHs emitted from PNe and post-AGB stars hosted by low-metallicity galaxies. There might be a slight difference, as no class $\mathcal{C}$ PAHs were found in LMC post-AGB stars, but confirmation is required with a larger sample in future. One possibility is that UV radiation in the general ISM and PNe might change the profiles of PAHs (Lebouteiller et al. 2011). An alternative process might be that PAHs in the ISM could be further re-processed within the ISM, changing the composition (Matsuura et al. 2013). This contrast of the ISM and PN PAH profiles could have potential in resolving how dust could be excited and processed in the circumstellar nebulae and ISM.

ACKNOWLEDGEMENTS

MM thanks Professor I. D. Howarth for his inputs about the classifications of high-mass stars. We thank Dr J. P. Searle for providing the Herschel measurements of IRAS 05189−7008 fluxes. Support for this research was provided by NASA through contract 1378453 issued by JPL/Caltech. This publication makes use of data products from the Two Micron All Sky Survey, which is a joint project of the University of Massachusetts and the Infrared Processing and Analysis Center/California Institute of Technology, funded by the National Aeronautics and Space Administration and the National Science Foundation. This research has made use of the SIMBAD data base, operated at CDS, Strasbourg, France. RSz acknowledges support from Marie Curie Actions IRSES (project No. 269193) of EU and from Polish NCN grant 2011/01/B/ST9/02031. FK acknowledges financial support from the National Science Council under grant number NSC100-2112-M-001-023-MY3. RS's contribution to the research described here was carried out at the Jet Propulsion Laboratory, California Institute of Technology, under a contract with NASA, and supported via an award issued by JPL/Caltech in support of his Spitzer Guest Observer programme.

REFERENCES

Alcock C. et al., 2001, ApJ, 554, 298
Allamandola L. J., Tielens A. G. G. M., Barker J. R., 1989, ApJS, 71, 733
Allen D. A., Swings J. P., 1976, A&A, 47, 293
Aoki W., Tsuji T., Ohnaka K., 1999, A&A, 350, 945
Bakker E. J., van Dishoeck E. F., Waters L. B. F. M., Schoenmaker T., 1997, A&A, 323, 469
Bauschlicher C. W. et al., 2010, ApJS, 189, 341
Bernard-Salas J., Peeters E., Sloan G. C., Cami J., Guiles S., Houck J. R., 2006, ApJ, 652, L29
Bernard-Salas J., Peeters E., Sloan G. C., Gutenkunst S., Matsuura M., Tielens A. G. G. M., Zijlstra A. A., Houck J. R., 2009, ApJ, 699, 1541
Blanco V. M., Blanco B. M., McCarthy M. F., 1980, ApJ, 242, 938
Blum R. D. et al., 2006, AJ, 132, 2034
Boersma C., Bouwman J., Lahuis F., Van Kerckhoven C., Tielens A. G. G. M., Waters L. B. F. M., Henning T., 2008, A&A, 484, 241
Boersma C., Bauschlicher C. W., Jr, Allamandola L. J., Ricca A., Peeters E., Tielens A. G. G. M., 2010, A&A, 511, A32
Botticella M. T. et al., 2009, MNRAS, 398, 1041
Breysacher J., Azzopardi M., Testor G., 1999, A&AS, 137, 117
Buchanan C. L., Kastner J. H., Hrivnak B. J., Sahai R., 2009, AJ, 138, 1597
Cami J., Bernard-Salas J., Peeters E., Malek S. E., 2010, Science, 329, 1180
Carpentier Y. et al., 2012, A&A, 548, A40
Cerrigone L., Hora J. L., Umana G., Trigilio C., 2009, ApJ, 703, 585
Cerrigone L., Hora J. L., Umana G., Trigilio C., Hart A., Fazio G., 2011, ApJ, 738, 121
Cherchneff I., Barker J. R., Tielens A. G. G. M., 1992, ApJ, 401, 269
Cioni M.-R. L., Marquette J.-B., Loup C., Azzopardi M., Habing H. J., Lasserre T., Lesquoy E., 2001, A&A, 377, 945
Clayton G. C. et al., 2011, ApJ, 743, 44
Cohen M., Jones B. F., 1987, ApJ, 321, L151
Cox A. N., 2000, Allen's Astrophysical Quantities. Springer, Berlin
Crowther P., De Marco O., Barlow M., 1998, MNRAS, 296, 367
Draine B. T. et al., 2007, ApJ, 663, 866
Duley W. W., Williams D. A., 1981, MNRAS, 196, 269
Egan M. P., Van Dyk S., Price S., 2001, AJ, 122, 1844
Elias J. H., Frogel J. A., Schwering P. B. W., 1986, ApJ, 302, 675
Furlan E. et al., 2006, ApJS, 165, 568
Furlan E. et al., 2008, ApJS, 176, 184
Gielen C. et al., 2009, A&A, 508, 1391
Gielen C., Cami J., Bouwman J., Peeters E., Min M., 2011, A&A, 536, A54
Gruendl R. A., Chu Y.-H., 2009, ApJS, 184, 172
Gruendl R. A., Chu Y.-H., Seale J. P., Matsuura M., Speck A. K., Sloan G. C., Looney L. W., 2008, ApJ, 688, L9
Herwig F., 2005, ARA&A, 43, 435
Higdon S. J. U. et al., 2004, PASP, 116, 975
Hony S., Van Kerckhoven C., Peeters E., Tielens A. G. G. M., Hudgins D. M., Allamandola L. J., 2001, A&A, 370, 1030
Houck J. R. et al., 2004, ApJS, 154, 18
Hrivnak B. J., Kwok S., Volk K. M., 1989, ApJ, 346, 265
Hrivnak B. J., Volk K. M., Kwok S., 2000, ApJ, 535, 275
Hrivnak B. J., Volk K. M., Kwok S., 2009, ApJ, 694, 1147
Hu J. Y., Slijkhuis S., de Jong T., Jiang B. W., 1993, A&AS, 100, 413
Hudgins D. M., Sandford S. A., 1998, J. Phys. Chem. A, 102, 344
Hughes S. M. G., 1989, AJ, 97, 1634
Humphreys R. M., Davidson K., 1994, PASP, 106, 1025
Jacoby G. H., 1980, ApJS, 42, 1
Jacoby G. H., Hunter D. A., Christian C. A., 1984, ApJS, 56, 257
Jones A. P., Duley W. W., Williams D. A., 1990, MNRAS, 31, 567
Jones O. C. et al., 2013, MNRAS, 427, 3209
Kastner J. H., Buchanan C. L., Sargent B., Forrest W. J., 2006, ApJ, 638, L29
Kato D. et al., 2007, PASJ, 59, 615
Keller L. D. et al., 2008, ApJ, 684, 411
Kemper F. et al., 2010, PASP, 122, 683
Kennicutt R. C., Jr et al., 2003, PASP, 115, 928
Klochkova V. G., Szczerba R., Panchuk V. E., Volk K. M., 1999, A&A, 345, 905
Klochkova V. G., Yushkin M. V., Miroshnichenko A. S., Panchuk V. E., Bjorkman K. S., 2002, A&A, 392, 143
Kontizas E., Dapergolas A., Morgan D. H., Kontizas M., 2001, A&A, 369, 932

Kraemer K. E., Sloan G. C., Bernard-Salas J., Price S. D., Egan M. P., Wood P. R., 2006, ApJ, 652, L25
Kwok S., Zhang Y., 2011, Nature, 479, 80
Kwok S., Hrivnak B. J., Geballe T. R., 1994, in Clegg R. E. S., Stevens I. R., Meikle W. P. S., eds, Circumstellar Media in Late Stages of Stellar Evolution. Cambridge Univ. Press, Cambridge, p. 296
Kwok S., Volk K. M., Bernath P., 2001, ApJ, 554, L87
Lambert D. L., Rao N. K., Pandey G., Ivans I. I., 2001, ApJ, 555, 925
Lamers H. J. G. L. M., Zickgraf F.-J., de Winter D., Houziaux L., Zorec J., 1998, A&A, 340, 117
Lebouteiller V., Bernard-Salas J., Sloan G. C., Barry D. J., 2010, PASP, 122, 231
Lebouteiller V., Bernard-Salas J., Whelan D. G., Brandl B., Galliano F., Charmandaris V., Madden S., Kunth D., 2011, ApJ, 728, 45
Leger A., Puget J. L., 1984, A&A, 137, L5
Leisy P., Dennefeld M., 1996, A&AS, 116, 95
Li A., Liu J. M., Jiang B. W., 2013, ApJ, 777, 111
Madden S. C., Galliano F., Jones A. P., Sauvage M., 2006, A&A, 446, 877
Matsuura M. et al., 2004, ApJ, 604, 791
Matsuura M. et al., 2005, A&A, 434, 691
Matsuura M. et al., 2006, MNRAS, 371, 415
Matsuura M. et al., 2009, MNRAS, 396, 918
Matsuura M., Woods P. M., Owen P. J., 2013, MNRAS, 429, 2527
Meixner M. et al., 2006, AJ, 132, 2268
Messenger S. J., Speck A., Volk K. M., 2013, ApJ, 764, 142
Molster F. J., Waters L. B. F. M., Tielens A. G. G. M., 2002, A&A, 382, 222
Morris P. W. et al., 1999, Nature, 402, 502
Moutou C., Léger A., D'Hendecourt L., 1995, Planet. Space Sci., 43, 1283
Moutou C., Leger A., D'Hendecourt L., 1996, A&A, 310, 297
Oliveira J. M. et al., 2009, ApJ, 707, 1269
Olszewski E. W., Suntzeff N. B., Mateo M. L., 1996, ARA&A, 34, 511
Peeters E., Hony S., Van Kerckhoven C., Tielens A. G. G. M., Allamandola L. J., Hudgins D. M., Bauschlicher C. W., 2002, A&A, 390, 1089
Peeters E., Allamandola L. J., Hudgins D. M., Hony S., Tielens A. G. G. M., 2004, in Witt A. N., Clayton G. C., Draine B. T., eds, ASP Conf. Ser. Vol. 309, Astrophysics of Dust. Astron. Soc. Pac., San Francisco, p. 141
Perea-Calderón J. V., García-Hernández D. A., Garcia-Lario P., Szczerba R., Bobrowsky M., 2009, A&A, 495, L5
Prieto J. P. et al., 2008, ApJ, 681, L9
Prieto J. P., Sellgren K., Thompson T. A., Kochanek C. S., 2009, ApJ, 705, 1425
Reid N., Glass I. S., Catchpole R. M., 1988, MNRAS, 232, 53
Rodgers A. W., Conroy P., Bloxham G., 1988, PASP, 100, 626
Sánchez Contreras C., Sahai R., Gil de Paz A., Goodrich R., 2008, ApJS, 179, 166
Sanduleak N., Philip A. G. D., 1977, PASP, 89, 792
Sanduleak N., MacConnell D. J., Philip A. G. D., 1978, PASP, 90, 621
Shimonishi T., Onaka T., Kato D., Sakon I., Ita Y., Kawamura A., Kaneda H., 2008, ApJ, 686, L99
Shimonishi T., Onaka T., Kato D., Sakon I., Ita Y., Kawamura A., Kaneda H., 2010, A&A, 514, A12
Skrutskie M. F. et al., 2006, AJ, 131, 1163
Sloan G. C., Kraemer K. E., Price S. D., Shipman R. F., 2003, ApJS, 147, 379
Sloan G. C. et al., 2007, ApJ, 664, 1144
Smith J. D. T., Houck J. R., 2001, AJ, 121, 2115
Smith G. et al., 2004, Proc. SPIE, 5492, 410
Smith N. et al., 2009, ApJ, 697, L49
Smolders K. et al., 2010, A&A, 514, L1
Socrates G., 2001, Infrared and Raman Characteristic Group Frequencies: Tables and Charts, 2nd edn. Wiley, West Sussex, England
Soszyński I. et al., 2009, Acta Astron., 59, 335
Speck A. K., Corman A. B., Wakeman K., Wheeler C. H., Thompson G., 2009, ApJ, 691, 1202
Stanghellini L., García-Lario P., García-Hernández D. A., Perea-Calderón J. V., Davies J. E., Manchado A., Villaver E., Shaw R. A., 2007, ApJ, 671, 1669
Suárez O., García-Lario P., Manchado A., Manteiga M., Ulla A., Pottasch S. R., 2006, A&A, 458, 173
Szczerba R., Siódmiak N., Stasińska G., Borkowski J., 2007, A&A, 469, 799
Thompson T. A., Prieto J. L., Stanek K. Z., Kistler M. D., Beacom J. F., Kochanek C. S., 2009, ApJ, 705, 1364
Tielens A. G. G. M., 2008, ARA&A, 46, 289
Tisserand P. et al., 2009, A&A, 501, 985
van Aarle E., Van Winckel H., Lloyd Evans T., Ueta T., Wood P. R., Ginsburg A. G., 2011, A&A, 530, 90
van der Hucht K. A. et al., 1996, A&A, 315, L193
van Diedenhoven B., Peeters E., Van Kerckhoven C., Hony S., Hudgins D. M., Allamandola L. J., Tielens A. G. G. M., 2004, ApJ, 611, 928
Van Genderen A. M., 2001, A&A, 366, 508
Van Kerckhoven C. et al., 2000, A&A, 357, 1013
van Loon J. T., Marshall J. R., Cohen M., Matsuura M., Wood P. R., Yamamura I., Zijlstra A. A., 2006, A&A, 447, 971
Van Winckel H., 2003, ARA&A, 41, 391
Van Winckel H., Reyniers M., 2000, A&A, 354, 135
Vassiliadis E., Wood P. R., 1993, ApJ, 413, 641
Vassiliadis E., Wood P. R., 1994, ApJS, 92, 125
Volk K. M., Kwok S., Hrivnak B. J., Szczerba R., 2002, ApJ, 567, 412
Volk K. M. et al., 2011, ApJ, 735, 127
Voors R. H. M., Waters L. B. F. M., Morris P. W., 1999, in Wolf B., Stahl O., Fullerton A. W., eds, IAU Colloq. 169, Variable and Non-Spherical Stellar Winds in Luminous Hot Stars. Springer, Berlin, p. 279
Voors R. H. M. et al., 2000, A&A, 356, 501
Waters L. B. F. M. et al., 1998, Nature, 391, 868
Werner M. W. et al., 2004, ApJS, 154, 1
Wesson R. et al., 2010, MNRAS, 403, 474
Westerlund B. E., 1997, The Magellanic Clouds. Cambridge Univ. Press, Cambridge
Westerlund B. E., Olander N., Hedin B., 1981, A&AS, 43, 267
Wood P. R., Cohen M., 2001, in Szczerba R., Górny S. K., eds, Astrophys. Space Sci. Libr. Vol. 265, MSX Sources in the LMC: Dust-Enshrouded AGB Stars and Post-AGB Stars. Kluwer, Dordrecht, p. 71
Wood P. R., Bessell M. S., Fox M. W., 1983, ApJ, 272, 99
Wood P. R., Bessell M. S., Paltoglou G., 1985, ApJ, 290, 477
Woods P. M. et al., 2011, MNRAS, 411, 1597
Zhang Y., Kwok S., Hrivnak B. J., 2010, ApJ, 725, 990
Zijlstra A. A. et al., 2006, MNRAS, 370, 1961

APPENDIX A: COLOUR–COLOUR AND COLOUR–MAGNITUDE DIAGRAMS

We have already presented one of the representative colour–colour diagrams used for the target selection in Section 4; the remaining diagrams are presented here.

A1 Colour–colour diagram J–[8.0] versus [8.0]–[24]

Fig. A1 shows the J–[8.0] versus [8.0]–[24] colour–colour diagram. Post-AGB stars have red mid-IR colours, [8.0]–[24] > 1.8.

van Aarle et al. (2011) used the [8.0]–[24] colour to find post-AGB candidates, and set the criteria of post-AGB to be [8.0]–[24] $>$ 1.384. Fig. A1 shows that all of our post-AGB stars fulfil this condition, but our sample proposes a redder cutoff at [8.0]–[24] $>$ 1.8.

Although the size of the current sample is limited, Fig. A1 suggests that the [8.0]–[24] colour can distinguish three types of objects; carbon-rich post-AGB stars, oxygen-rich post-AGB stars and carbon-rich AGB stars. Oxygen-rich post-AGB stars have a colour range of $1.8 <$ [8.0]–[24] < 3.5, whereas carbon-rich post-AGB stars have [8.0]–[24] > 3.5, and carbon-rich AGB stars have bluer colours with [8.0]–[24] < 2. The difference is due to the dust properties of these three types of objects.

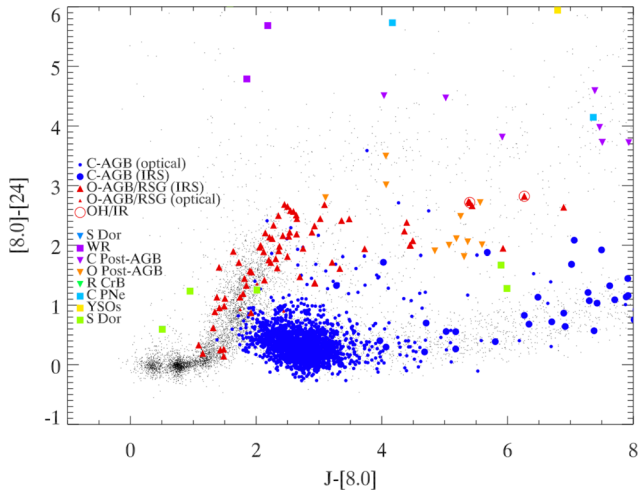

Figure A1. The J–[8.0] versus [8.0]–[24] colour–colour diagram. Post-AGB stars fall in the red part of the diagram (J–[8.0] > 3.0 and [8.0]–[24] > 1.8).

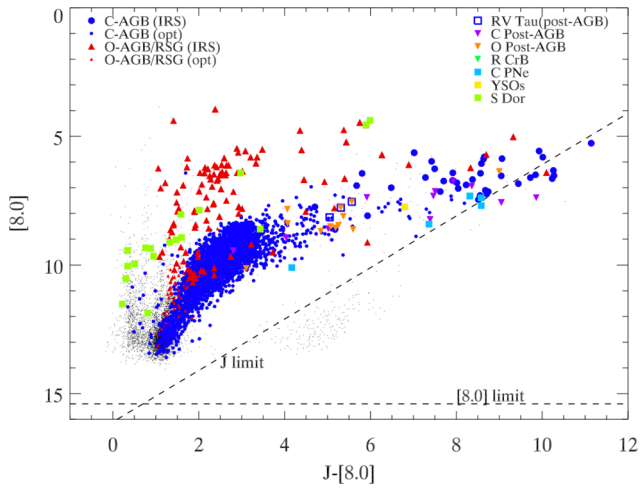

Figure A2. Colour–magnitude diagram J–[8.0] versus [8.0], which was used for part of the target selection. The oxygen-rich post-AGB stars fall in a small range, $3 < J$–[8.0] < 6 and $7 <$ [8.0] < 10, with the exception of one star at J–[8.0] ~ 8.5. Carbon-rich post-AGB stars are found in the range of J–[8.0] > 7 and $6 <$ [8.0] < 9. Post-AGB stars tend to have similar colours to red AGB stars in this diagram. *Spitzer* and 2MASS detection limits are plotted as dashed lines.

We used the criteria of J–[8.0] > 5 and [8.0]–[24] > 0.5 to select carbon-rich AGB stars. We found that the colour distributions of carbon-rich post-AGB stars are slightly bluer in J–[8.0] (>4), but redder in [8.0]–[24] (>3.5).

A2 Colour–magnitude diagrams

We examine the colour–magnitude diagrams, used for the selection of post-AGB stars. Fig. A2 shows the J–[8.0] versus [8.0] colour–magnitude diagram: post-AGB stars have $J - [8.0] > 4$, except for one object and $5 <$ [8.0] < 10. Similarly, Fig. A3 shows the [4.5] − [8.0] versus [8.0] colour–magnitude diagram, where carbon-rich post-AGB stars are found at [4.5] − [8.0] > 3. However, these diagrams suffer from contaminations by other types of object, particularly carbon-rich AGB stars. After the selection of post-AGB

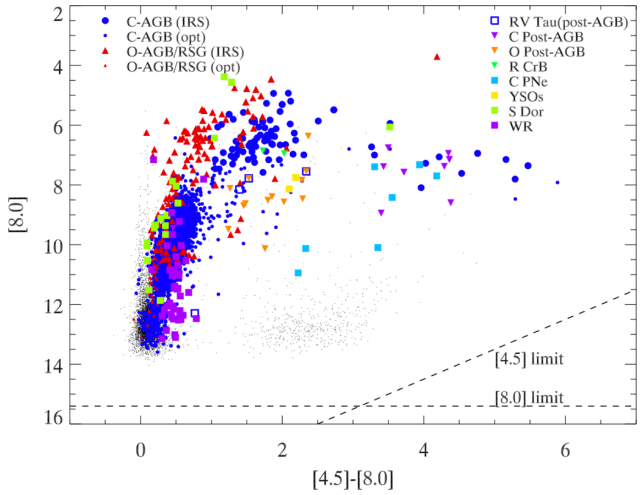

Figure A3. Colour–magnitude diagram [4.5]–[8.0] versus [8.0], which was used for part of the target selection. Oxygen-rich post-AGB stars fall in the ranges $1 <$ [4.5]–[8.0] < 2.5 and $6 <$ [8.0] < 10, fainter than IR-selected oxygen-rich AGB stars and supergiants. Carbon-rich post-AGB stars have much redder colours than oxygen-rich post-AGB stars, having $3 <$ [4.5]–[8.0] < 5. Carbon-rich post-AGB stars and carbon-rich PNe have similar colours.

candidates, spectroscopic follow-up observations are essential to reveal their true nature.

A3 The [3.6]–[4.5] versus [4.5] colour–magnitude diagram

The colour–magnitude diagram [3.6]–[4.5] versus [4.5] is often used to identify AGB stars/post-AGB stars in nearby galaxies (e.g. Thompson et al. 2009), because these two *Spitzer* wavebands tend to contain more stars than the other two *Spitzer* IRAC ([5.8] and [8.0]) bands.

The particular interest of the [3.6]–[4.5] versus [4.5] diagram is because it was used to diagnose the evolutionary stage of the progenitor star of supernova (SN) 2008S, which could be an AGB star or a post-AGB star (Botticella et al. 2009; Prieto et al. 2009; Smith et al. 2009; Wesson et al. 2010). The explosion of SN 2008S was detected in the spiral galaxy NGC 6946, and its progenitor star was found in the *Spitzer* image of NGC 6946 taken before the explosion. From *Spitzer* photometric data, Thompson et al. (2009) proposed that the progenitor star should be a high-mass star but within the relatively low-mass range (8–12 $M_{\odot}$). Wesson et al. (2010) suggested that it could be a carbon-rich AGB star or super-AGB star with a mass range of 6–10 $M_{\odot}$. Prieto et al. (2008, 2009) proposed that the progenitor of SN 2008S is a carbon-rich post-AGB star, from the presence of Ca II emission in the optical spectra and from the IR colour showing a carbon-rich circumstellar envelope.

The carbon-rich AGB/post-AGB possibility for the progenitor of SN 2008S can be assessed by comparing the colour–magnitude diagrams of our spectroscopically classified objects in the LMC. The progenitor of SN 2008S had a colour of [3.6]–[4.5] > 1.5 and the absolute luminosity of $M_{4.5} < -10$ (Prieto et al. 2008). This 4.5 μm absolute magnitude corresponds to an apparent magnitude of [4.5] < 8.5 for the LMC distance, assuming the distance module of 18.5 mag for the LMC. The corresponding colour and magnitude of the SN 2008S progenitor scaled to the LMC distance is indicated as the dashed-line box in Fig. A4. Two carbon-rich stars and one oxygen-rich RSG, which is IRAS 05346−6949 (Elias, Frogel & Schwering 1986), are found within this box. No known S Dor or WR stars fall within this box, neither are there any post-AGB stars

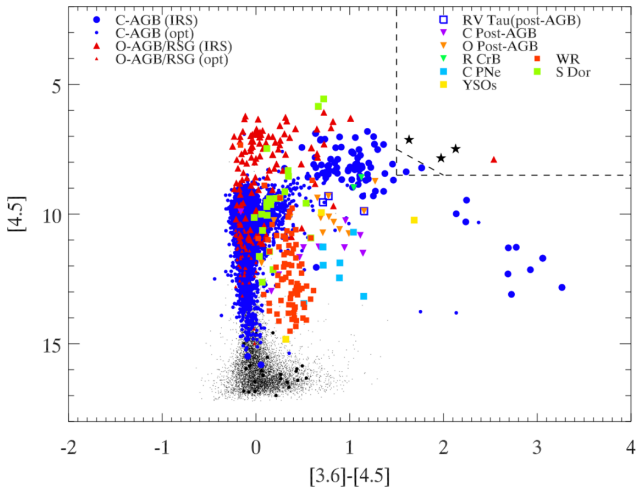

Figure A4. Colour–magnitude diagram [3.6]–[4.5] versus [4.5], which has been used for object classifications. The box shows the region where the progenitors of SN 2008S can be found. Among several possibilities, this diagram suggests that carbon-rich AGB stars or oxygen-rich RSGs are the most likely object types.

or PNe. There are three unclassified objects, indicated by 'star' symbols, within the box. From this colour–magnitude diagram, the colour corresponding to the progenitor of SN 2008S, seems to have been either a carbon-rich AGB star or an oxygen-rich RSG, but is less likely to have been a post-AGB star.

APPENDIX B: DEMONSTRATION OF THE SMALL INFLUENCE OF THE CONTINUUM ON THE PEAK WAVELENGTHS OF THE 6–9 μM FEATURES

The continuum subtraction may potentially distort the features, raising concern that the PAH classification of the profiles $\mathcal{C}$ and $\mathcal{D}$ of the broad 7.5–9 μm features might be caused by poor continuum subtraction. In order to establish that the distinction of profiles $\mathcal{C}$ and $\mathcal{D}$ is indeed present, Fig. B1 shows the observed spectra and the continuum divided spectra of the representative class $\mathcal{C}$ and class $\mathcal{D}$ objects. IRAS 13416−6243 is a Galactic post-AGB star with a class $\mathcal{C}$ PAH profile in the 6–9 μm range, showing a broad single peak at 8.22 μm. IRAS 05110−6616 is an LMC class $\mathcal{D}$ object, that also has a broad feature between 7.5 and 9 μm range, but with the peak at a shorter wavelength than in class $\mathcal{C}$.

In our analysis, we used the continuum-subtracted spectra. In order to demonstrate that the continuum subtraction did not create an artificial distinction between class $\mathcal{C}$ and class $\mathcal{D}$ profiles, Fig. B1(b) displays the continuum divided spectra. A rising continuum, if the continuum is more dominant than the features, could potentially shift the peak wavelengths of the features towards longer wavelengths, but this effect could be cancelled out better in continuum-divided spectra than in continuum-subtracted spectra. Fig. B1(b) demonstrates that class $\mathcal{C}$ and class $\mathcal{D}$ objects clearly have different peak wavelengths of the 7.5–9 μm broad feature.

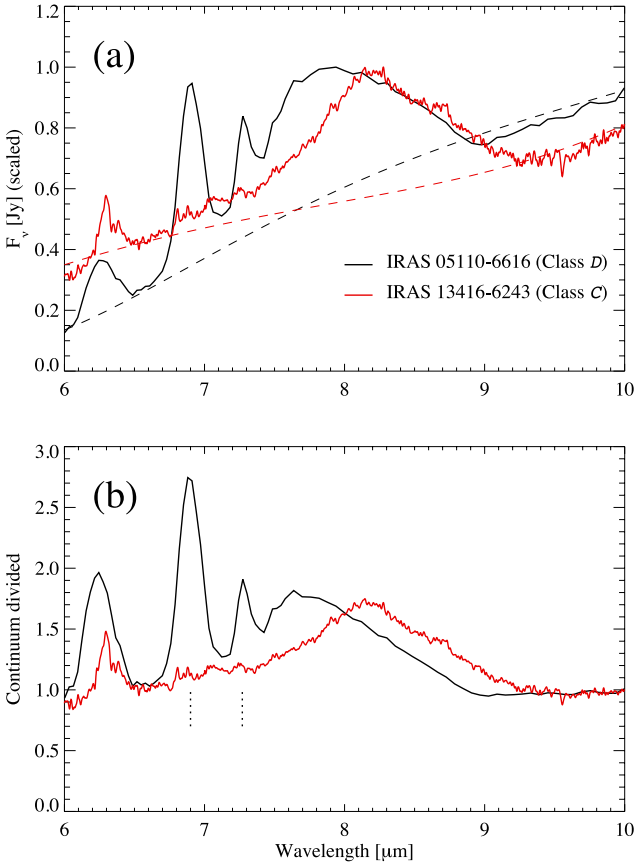

Figure B1. Demonstration of the small influence of the continuum definitions on the peak wavelengths of the broad 7.5–9 μm features. Panel (a) shows the observed spectra of IRAS 05110−6616 (LMC class-$\mathcal{D}$ object) and IRAS 13416−6243 (Galactic class-$\mathcal{C}$ object), along with their continua in dashed lines. The fluxes are scaled to the peak value within the 6–9 μm range. The spectrum of IRAS 05110−6616 indicates the peak at about 7.8–7.9 μm, whereas the peak is found at 8.2 μm for IRAS 13416−6243. Panel (b) indicates the continuum-divided spectra, instead of continuum-subtracted spectra, which were used in the PAH analysis. Comparisons of these two spectra show that the difference in the peak wavelengths of these two spectra remain even in continuum-divided spectra. Note that the spectrum of IRAS 05110−6616 has in addition two narrow features at ∼6.9 and ∼7.3 μm, apart from the broad feature at 7.5–9 μm region.

APPENDIX C: OPTICAL SPECTRA

Optical spectra of four objects (IRAS 04589−6547, J052520.75−705007.3, J054055.81−691614.6 and MSX LMC 1795) were obtained with the Blanco 4-m telescope using the RC Spectrograph on 2010 January 27, and their spectra are shown in Fig. C1. The spectrograph employed the KPGL2-1 grating (316 lines mm^{-1}), and the resulting spectrum was imaged by the blue Air Schmidt Camera and Loral 3k (# 1) CCD. The 150 μm (1 arcsec) wide long slit was oriented in the east–west direction. The resulting spectra were sampled with ∼2Å $pixel^{-1}$, and have an effective spectral resolution of ∼750 (∼8.5 Å) at Hα (as measured from unresolved sky lines). The observations were reduced using the CCDPROC and TWODSPEC packages in IRAF. Each spectrogram was overscan and bias corrected, then the wavelength calibration, based on exposures of a HeNeAr lamp taken just prior to or after those for the source, and a spatial distortion correction were applied to each spectrogram.

The spectrum of J052520.75−705007.3 in Fig. C1 shows strong Ca II H&K, weak *G* band, sharp weak H line absorption and strong O I 7774 Å, giving a spectral type of F2–F5I, with reference to the spectral atlas of Jacoby, Hunter & Christian (1984). This is significantly later than the type A1Ia (van Aarle et al. 2011), based on a red spectrum with an undetectable Ca II triplet.

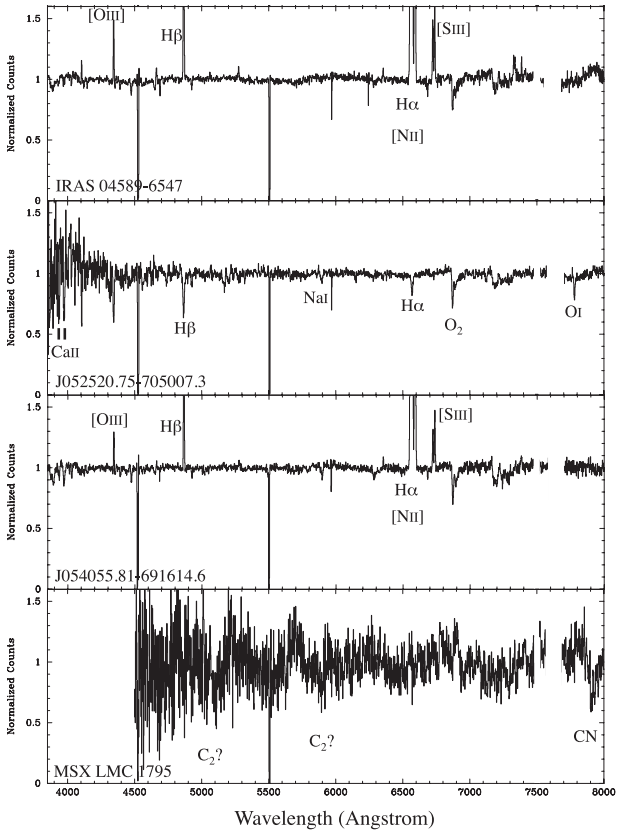

Figure C1. Normalized optical spectra of four objects, IRAS 04589−6547, J052520.75−705007.3, J054055.81−691614.6 and MSX LMC 1795.

The spectrum of MSX LMC 1795 has a moderately strong red CN band and a possible C_2 Swan band at 5165 Å and CN, showing it is a carbon star, consistent with our classification of the mid-IR spectrum as typical of an R CrB star. The lack of coverage in the blue spectral region and the low S/N preclude inspection of the features diagnostic of an R CrB star. The 2MASS, 6X2MASS and IRSF photometry show a considerable spread, because of a faint blue companion at about 1 arcsec distance which affects J as well as intrinsic variability. All three data sets show it is a very red star which clearly lies in the R CrB rather than the DY Per zone in the two colour diagram (Tisserand et al. 2009), so it is an R CrB star and not a DY Per star or a C-rich AGB star.

The optical spectra of IRAS 04589−6547 in our Fig. C1 and in van Aarle et al. (2011) give a spectral type O9ep/B1-2ep, while that of J054055.81−691614.6 is O–B. Both stars have intense Hα emission, and the equivalent widths (EWs) of the emission lines have been measured with one or more of the instruments described in this section and the Unit Spectrograph on the 1.9-m Radcliffe reflector at South African Astronomical Observatory (SAAO), which gave a resolution of 4–5 Å depending on wavelength. The EW values are given for IRAS 04589−6547 first: [O II] 3727 Å: 5.4, 0.8, Hδ: 1.0, 0.3, Hγ: 3.4, 1.9, Hβ: 15.2, 9.4, Hα: 132, 102, [N II] 6548 Å: 20, 24, [N II] 6584 Å: 62, 76, [S II] 6717 Å: 3.1, 2.0, [S II] 6731 Å: 5.1, 3.3, OI 8446 Å: 1.4, 1.8 and [S III] 9069 Å: 23, 10. Observations on different dates give no indication of variability in these line strengths.

Optical spectra of five objects were observed with the Anglo-Australian Telescope (AAT) or the 2.3-m telescope of the Australian National University at Siding Spring Observatory, and their spectra are shown in Fig. C2. The spectra of IRAS 05189−7008 and

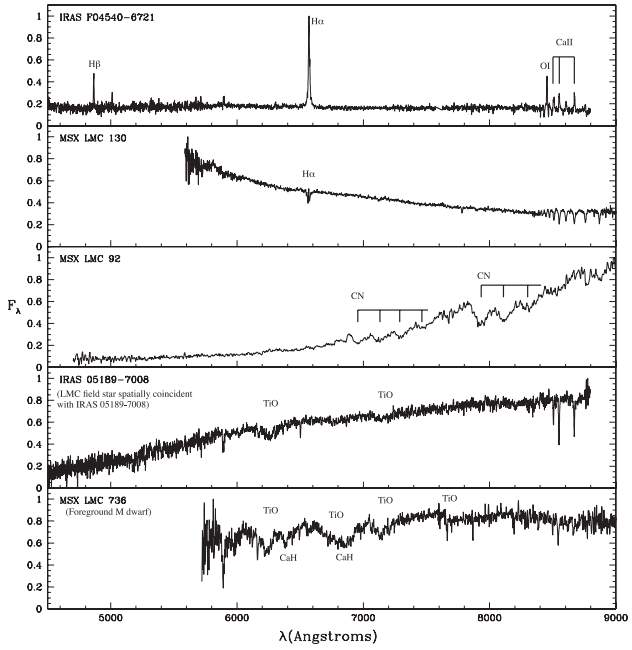

Figure C2. Optical spectra for five objects, showing relative F_λ versus λ. The optical spectra of IRAS 05189−7008 and MSX LMC 736 are not those of the mid-IR sources, but correspond to field stars in the same line of sight.

IRAS F04540−6721 were taken with the AAT on 2010 October 28 and 29, respectively, using the multifibre AAOmega spectrograph (Smith et al. 2004) with a resolution of ∼1300. The spectra of MSX LMC 130 and MSX LMC 736 were taken on 2000 January 13 using the Dual-Beam Spectrograph (Rodgers, Conroy & Bloxham 1988) on the 2.3-m telescope. The spectra have a resolution of ∼2000. MSX LMC 92 was observed with the same telescope and instrument on 2003 December 25 at a lower resolution of ∼1000. In all the spectra, telluric features have been removed by dividing the spectra by the spectrum of a featureless white dwarf.

IRAS F04540−6721 is an emission line star showing emission lines of H I (Hα and Hβ), O I (8446 Å), Na I (5889,5895 Å) and Ca II (8498, 8542, 8662 Å). Possible [O III] (5007 Å) could be from the LMC field. MSX LMC 130 has a spectral type of about A7, with Hα in emission in the core of the absorption line. MSX LMC 92 is a cool carbon star as shown by the characteristic CN bands.

The optical spectra of two stars were found to be those of field stars which are spatially coincident with the mid-IR sources. The optical counterpart to IRAS 05189−7008 shows weak TiO bands near 6250 and 7050 Å, so it is an O-rich star of type near K4. JHK_s photometry from the IRSF, 2M and 6X2M give concordant results, $J - H = 0.84$, $H - K_s = 0.19$, in agreement with the type. The offset from the catalogue position of 1.0 arcsec may be significant. The optical counterpart to MSX LMC 736 shows strong CaH bands near 6380 and 6850 Å, as well as TiO bands, and it appears to be an M dwarf (M1V), located in the foreground of the LMC. The positional offset is zero in this case, and the IRSF, 2M and 6X2M photometry obtained at different epochs give ranges of 0.01, 0.08 and 0.53 mag at J, H and K_s, respectively. This is consistent with an increasing contribution from a variable AGB star towards longer wavelength. The near-IR photometry of these two stars was not used in Fig. 1, in view of the contamination by field stars.

This paper has been typeset from a TEX/LATEX file prepared by the author.